https://doi.org/10.5194/acp-2021-536
Preprint. Discussion started: 6 July 2021

Atmospheric Chemistry and Physics Discussions

Quantifying urban, industrial, and background changes in NO_2 during the COVID-19 lockdown period based on TROPOMI satellite observations

Vitali Fioletov[1], Chris A. McLinden[1], Debora Griffin[1], Nickolay Krotkov[2], Fei Liu[2], Henk Eskes[3]

[1]Air Quality Research Division, Environment and Climate Change Canada, Toronto, Canada
[2]Atmospheric Chemistry and Dynamics Laboratory, NASA Goddard Space Flight Center, Greenbelt, Maryland, USA
[3]Environmental Sciences Group, Wageningen University, Wageningen, the Netherlands

Correspondence to: Vitali Fioletov (Vitali.Fioletov@outlook.com or Vitali.Fioletov@canada.ca)

Abstract. The COVID-19 lockdown had a large impact on anthropogenic emissions of air pollutants and particularly on nitrogen dioxide (NO_2). While the overall NO_2 decline over some large cities is well-established, its quantification remains a challenge because of a variety of sources of NO_2. In this study, a new method of isolation of three components: background NO_2, NO_2 from urban sources, and from industrial point sources is applied to estimate the COVID-19 lockdown impact on each of them. The approach is based on fitting satellite data by a statistical model with empirical plume dispersion functions driven by the observed winds. Population density and surface elevation data as well as coordinates of industrial sources were used in the analysis. The NO_2 vertical column density (VCD) values measured by Tropospheric Monitoring Instrument (TROPOMI) on board Sentinel-5 Precursor over 263 urban areas for the period from March 16 to June 15, 2020, were compared with the average VCD values for the same period in 2018 and 2019. While background NO_2 component remained almost unchanged, the urban NO_2 component declined by 18-28% over most regions. India, South America, and a part of Europe (particularly, Italy, France, and Spain) demonstrated a 40-50% urban emissions decline. In contrast, decline over urban area in China, where the lockdown was over during the analyzed period, was only 3% except for Wuhan, where more than 60% decline was observed. Emissions from large industrial sources in the analyzed urban areas varies largely from region to region from +5% for China to -40% for India. Changes in urban emissions are correlated with changes in Google mobility data (the correlation coefficient is 0.66) confirming that changes in traffic was one of the key elements in decline of urban NO_2 emissions. No correlation was found between changes in background NO_2 and Google mobility data.

https://doi.org/10.5194/acp-2021-536
Preprint. Discussion started: 6 July 2021

Atmospheric Chemistry and Physics Discussions

1 Introduction

Nitrogen oxides (NO_x =NO_2 + NO) are air pollutants that originate from various anthropogenic (fuel combustion) and natural (e.g., biomass burning, lightning) sources and NO_x emissions are regulated in many countries. One component of NO_x, NO_2 has a long history of satellite measurements. In the stratosphere, the SAGE (Stratospheric Aerosol and Gas Experiment) instrument provided NO_2 profile information through the stratosphere beginning in the mid-1980s (Cunnold et al., 1991). Satellite observations of tropospheric NO_2 columns are more recent and began with the nadir-viewing GOME (Global Ozone Monitoring Experiment) in 1996 (Martin et al., 2002) with several successors, chief among these OMI (Ozone Monitoring Instrument) (Duncan et al., 2015; Krotkov et al., 2016; Lamsal et al., 2015; Levelt et al., 2018) and, most recently, TROPOMI (Tropospheric Monitoring Instrument) (Van Geffen et al., 2020; Veefkind et al., 2012). Collectively these instruments have been used to better understand NO_2 sources, sinks, distributions, and trends (Beirle et al., 2011, 2019; Liu et al., 2016; Lorente et al., 2019; Lu et al., 2015; Martin et al., 2002; McLinden et al., 2012; Stavrakou et al., 2020; Vîrghileanu et al., 2020) .

One primary NO_2 characteristic provided by satellites is vertical column density (VCD), a geophysical quantity representing the total number of molecules or total mass per unit of area. The main features of the tropospheric NO_2 VCD distribution are well established. Due to its relatively short lifetime, a few hours within a plume at daytime, NO_2 is elevated near sources such as urban areas (Beirle et al., 2019; Lorente et al., 2019; Lu et al., 2015) and industrial sources such as power plants and oil refineries (Liu et al., 2016; McLinden et al., 2012). Over high mountains, NO_2 VCDs are relatively small as the troposphere there is "thinner" with fewer emission sources. Ship tracks and major highways also create elevated NO_2 values on satellite maps (Beirle et al., 2004; Georgoulias et al., 2020; Liu et al., 2020; Richter et al., 2004).

Satellite data are widely used to estimate emissions and lifetimes from large NO_2 point sources (Streets et al., 2013). Methods such as inverse modelling (Konovalov et al., 2006; Mijling and Van Der A, 2012) and, more recently, flux divergence (Beirle et al., 2019) are used for such purpose. One common approach is based on a rotation of satellite NO_2 pixels around the source to align the wind data to a common direction, integrating the data across the wind direction and then fitting the results with an exponentially modified Gaussian (EMG) function (Lange et al., 2021; Pommier et al., 2013). The two unknown parameters, the emission strength and lifetime are estimated directly from the fit in one-dimensional space. The method works well for isolated stationary point sources and with steady winds. Another approach employs a two-dimensional plume function of the wind speed (Dammers et al., 2019; Fioletov et al., 2015). The plume function depends on three parameters: the plume width, lifetime and emission strengths. While all three parameters can be estimated from the fit, the algorithm works better if the plume width and lifetime are estimated in advance and then their prescribed values are used to estimate the emission. This algorithm can be further improved to account for multiple sources (Fioletov et al., 2017).

The COVID-19 lockdown had an impact on the NO_2 emissions worldwide (Bao and Zhang, 2020; Bauwens et al., 2020; Ding et al., 2020; Gkatzelis et al., 2021; Kanniah et al., 2020; Keller et al., 2021; Koukouli et al., 2021; Liu et al., 2020; Vadrevu et al., 2020; Vîrghileanu et al., 2020; Zhang et al., 2021). It was demonstrated that NO_2 surface concentrations and VCDs have significantly declined in US and Canada after mid-March 2020 (Bauwens et al., 2020; Goldberg et al., 2020;

https://doi.org/10.5194/acp-2021-536
Preprint. Discussion started: 6 July 2021

Atmospheric Chemistry and Physics Discussions

Griffin et al., 2020). A decline of about 20%-25% was observed in US megacities, as well as over some rural areas. The results of satellite data analysis, however, may depend on the selected area around the city. Changes in industrial point source emissions could be different from urban emissions and there is also free tropospheric NO_2 (Silvern et al., 2019) that could mask the lockdown-related changes in anthropogenic emissions.

In this study, a new method of isolation of three main components: background NO_2, NO_2 from urban sources, and from industrial point sources is applied to estimate the COVID-19 lockdown impact on each of them. The algorithm is based on a multisource plume dispersion function fitting approach developed for SO_2 point and area sources (Fioletov et al., 2017; McLinden et al., 2020). It assumes that each source produces a plume that depends on unknown emission strength and these emission strengths are derived from the best fit to the satellite data. The algorithm was adapted for NO_2 where emissions from urban areas, which tend to be dominated by residential and mobile emission sources, were one of the major factors. Population density data were used as a proxy for such emissions (Lamsal et al., 2013). As the elevation of the landscape plays an important role in the NO_2 spatial distribution, it too was taken into account by the algorithm. Since the approach is based on statistical methods with a large number of parameters to estimate, it was necessary to have sufficiently long data set to reduce the impact of natural factors such as meteorology (Goldberg et al., 2020). Estimates for three month-long period from March 16 to June 15, 2020, are compared to similar estimates for the same period in 2018 and 2019 for 3° by 4° areas around 263 major cities worldwide. As the study is focused on relative NO_2 changes due to the lockdown, possible systematic errors related to the TROPOMI retrievals (Verhoelst et al., 2021) and the algorithm fitting parameters (Fioletov et al., 2016) play a much smaller role than in the case of absolute emission estimates.

This paper is organized as follows: Section 2 describes various data sets used in the study; the analysis algorithm is discussed in Section 3. In Section 4, the COVID-19 lockdown impact is studied. USA and Canada are analyzed in detail to illustrate the method, then statistics for Europe is provided and finally results for the entire world are presented. Discussion and conclusions are given in Section 5. The algorithm is described in Appendix. Additional technical information such as sensitivity analysis, the uncertainty estimates, and statistics for individual regions are given in the Supplement.

2 Data Sets

2.1 TROPOMI NO_2 VCD data

TROPOMI, onboard of the European Space Agency (ESA) and EU Copernicus Sentinel 5 Precursor (S5p) satellite, was launched on 13 October 2017 (Van Geffen et al., 2020; Veefkind et al., 2012). The satellite follows a Sun-synchronous, low-Earth (825 km) orbit with a daily equator crossing time of approximately 13:30 local solar time (van Geffen et al., 2019). At nadir, TROPOMI pixel sizes were 3.5 × 7 km^2 at the beginning operation and were reduced to 3.5 × 5.6 km^2 on 6 August 2019 and the swath width is 2,600 km. TROPOMI NO_2 VCD values represent the total number of molecules or total mass per unit area and are often given in molecules or moles (one mole is equal to 6.022×10^{23} molecules) per square metre or centimetre as well as in Dobson Units (DU, 1 DU = $2.69\bullet10^{16}$ molec•cm^{-2}). In this study, level 2 TROPOMI data available from the

https://doi.org/10.5194/acp-2021-536
Preprint. Discussion started: 6 July 2021


Atmospheric Chemistry and Physics Discussions

Copernicus open data access hub (https://s5phub.copernicus.eu) were used. The standard TROPOMI product, tropospheric vertical columns, based on air mass factors (AMFs) calculated using the vertical profile of NO_2 from the TM5-MP model at 1°×1° resolution (Williams et al., 2017) was used. In the analysis, we use only data for which the quality assurance value is higher than 0.75 (Van Geffen et al., 2018). Also, satellite pixels with snow on the ground, a solar zenith angle greater than 80 degrees and with cloud radiance fraction above 0.3 were excluded from the analysis.

The TROPOMI NO_2 distribution over the US and southern Canada is shown in Fig.1. The data are stratified by the wind speed to highlight some of the features of the NO_2 distribution. NO_2 values are elevated over large cities, as is particularly evident from the maps for low wind speed where the NO_2 remains close to the source before chemical or physical removal. Smaller values over elevated areas such as the Rocky Mountains and Appalachians and higher values over valleys such the California Central Valley are evident from the map. There is also some background NO_2 that can be seen even over remote areas with no major sources.

2.2 Wind data

As in several previous studies (Fioletov et al., 2015; McLinden et al., 2020; Zoogman et al., 2016) the plume dispersion function (discussed below in Sect. 3) is based on the wind speed and direction obtained from the meteorological reanalysis. For each satellite pixel, wind speed and direction were taken from European Centre for Medium-Range Weather Forecasts (ECMWF) ERA5 reanalysis data (C3S, 2017; Dee et al., 2011), which were merged with TROPOMI measurements. The wind profile data have one hour temporal resolution and are available on a 0.25° horizontal grid. U- and V- (west-east and south-north, respectively) wind-speed components were then interpolated to the location of the centre of each TROPOMI pixel and to overpass time. The wind components were averaged in the vertical between 0 and 1 km. The results are not very sensitive to the wind height within this range as was previously investigated by (Beirle et al., 2011) because the boundary layer wind is relatively constant, except close to the surface.

2.3 Elevation, emission, and population density data

The Gridded Population of the World (GPW) dataset (SEDAC, 2017) was used as a proxy for the urban component. GPW data are on 0.042 degree (2.5 arc-minute) grid and consists of estimates of human population density (number of persons per square kilometre) based on counts consistent with national censuses and population registers. Information about large city location and population, that was used to select cities for the analysis, was obtained from the World Cities Database available from https://simplemaps.com/data/world-cities (accessed on May 10, 2021). To verify the obtained results, another proxy, night lights, was used. The night lights data are from Visible Infrared Imaging Radiometer Suite (VIIRS) onboard Suomi National Polar-orbiting Partnership (NPP) available from https://earthobservatory.nasa.gov/features/NightLights/page3.php (accessed on May 10, 2021) (Miller et al., 2012).

Information about emission sources was used in two main ways. First, coordinates of selected sources were used to establish locations of point sources in the fitting algorithm. Second, location and emission strengths were used to calculate

https://doi.org/10.5194/acp-2021-536
Preprint. Discussion started: 6 July 2021

Atmospheric Chemistry and Physics Discussions

NO_2 VCD spatial distribution used for comparisons with satellite-based estimates. The analysis was done in three stages. The algorithms were originally developed and tested for the U.S. and Canada, then it was applied for Europe. For these regions, detailed information about emission sources was available. Finally, it was applied worldwide, where information about the emission sources was often limited.

For the U.S. and Canada, monthly point source NO_x emissions from the U.S. Environmental Protection Agency (EPA) National Emissions Inventory (NEI) (EPA, 2020) and annual emissions from the Canadian National Pollutant Release Inventory (NPRI, 2020) were used. Note that, unlike most of the other sources of emission information, the U.S. EPA emissions data are based on a continuous emissions monitoring system (CEMS), i.e., on real emission measurements. At the time of this study, the U.S. monthly emissions data were available up to October 2020. For Canadian sites, only annual emissions were available up to 2018 and so monthly values were calculated by dividing 2018 annual emissions by 12. Only sources with annual emissions >1 kt of NO_x per year were selected and used in this study.

Information about annual European emissions is available from European Pollutant Release and Transfer Register (https://prtr.eea.europa.eu/) (accessed on March 2, 2021). The emissions database includes two files: one with data for 2007-2017 and the most recent database for 2017-2019. However, the second database does not include data from many countries and the inventories are incomplete. For this reason, we used the data from the former database to establish locations of European point emission sources.

The world powerplant database (https://globalenergymonitor.org/projects/global-coal-plant-tracker/) was used to find locations of power plants for the global analysis. Note that for the analysis, only source locations, not emissions themselves, are required. Other sources that were detected from satellite data were then identified using satellite imaginary such as Google, Microsoft Bing, and Sentinel 2 maps.

Elevation data used in this study are from 0.03 degree (two-arc minute) gridded global relief ETOPO2v2 database (NOAA, 2006). Google Each Community Mobility Report data were obtained from https://www.google.com/covid19/mobility/ (accessed on March 2, 2021).

3 The Emissions fitting algorithms

This section provides only a general description of the method. The calculation formulas are given in the Appendix. The method is adapted from the previously designed algorithm for multi-sources SO_2 emission estimates (Fioletov et al., 2017) where the emissions are determined from the best fit of satellite observation by a set of plume functions (one per source) scaled by parameters of estimation representing the emission strength. Unlike SO_2, where emissions are mostly generated by point sources, NO_2 emissions also originate from area sources such as large cities. As shown in Fig.1, landscape also has a major impact on the NO_2 distribution. To accommodate these features, the statistical model from Fioletov et al (2017) was modified to:

$$TROPOMI\ NO_2 = \alpha_0 + \alpha_p \Omega_p + \Sigma\, \alpha_i \Omega_i + (\beta_0 + \beta_1(\theta - \theta_0) + \beta_2(\varphi - \varphi_0)) \cdot exp(-H/H_0) + \varepsilon \quad (1)$$

https://doi.org/10.5194/acp-2021-536
Preprint. Discussion started: 6 July 2021

Atmospheric Chemistry and Physics Discussions

where α_0, α_e, α_p, α_i, β_0, β_1, and β_2 are the unknown regression parameters representing population density-related proxies and emissions from individual point sources and a background with contribution from the elevation; Ω_p is the source plume function for the population density-related distributed source (or area source); Ω_i are the source plume functions for industrial point sources; H is the elevation above sea level and the scaling factor H_0=1 km was introduced to make the exponential argument dimensionless; and ε is the residual noise. The fitting was done for 3° by 4° areas around large cities by minimization of the squares of the residuals (ε). The fitting and parameter estimation was done using all individual level 2 pixels for the period from March 16 to June 15 three times: for 2018, 2019, and 2020. So, three sets of coefficients were obtained and then used to estimate the background levels and emissions. Then, the average results for 2018 and 2019 were compared with these for 2020.

As in Fioletov et al., 2017, the plume from a point source i is described by a plume function $\Omega(\theta, \varphi, \omega, s, \theta_i, \varphi_i)$ where θ and φ are the satellite pixel coordinates; ω and s are the wind direction and speed for that pixel; and θ_i and φ_i are the source coordinates. An unknown parameter (α_i) represents the total NO_2 mass emitted from the source i. The emission rate for source i can be expressed as $E_i = \alpha_i/\tau$, where τ is a prescribed NO_2 lifetime (or, more accurately, decay time, but we use the term "lifetime" because it is more common). Note that τ is different from the chemical lifetime (de Foy et al., 2015). Once the emission rate is established, it can be used to reconstruct how distribution of NO_2 emitted by that source would be seen by a satellite.

The plume functions Ω are EMG functions that are commonly used to approximate plumes of VCDs of trace gases such as NO_2, SO_2, and ammonia (Beirle et al., 2011, 2014; Dammers et al., 2019; Fioletov et al., 2017, 2015; de Foy et al., 2015; Liu et al., 2016; McLinden et al., 2020). Similar in concept to a Gaussian plume function, they also take into account the finite physical size of the source and the spatial resolution of the satellite instrument being utilized. The shape of the EMG function depends on the prescribed plume width (w) and the gas lifetime (τ) plus on an unknown emission strength of the plume α_p. In general, the plume width parameter depends on the size of the source and the size of satellite pixel. The value of 8 km for plume width was used in this study for TROPOMI along with a constant lifetime value of 3.3 hours. The switch from 7 to 5.6 km along-track resolution in 2019 might have some impact on the optimal plume width, but as the sensitivity analysis show that small changes in w have only a minor impact on the results (Supplement A). The lifetime reflects the rate at which NO_2 is removed from the plume due to chemical conversion or physical removal such as deposition; it depends on several factors such as season and NO_2 concentration. It is about 2-6 hours in summer and longer in winter (de Foy et al., 2014; Liu et al., 2016). Moreover, for some sources, the lifetime may be changing over time (Laughner and Cohen, 2019) as NO_2 concentration declines, although other studies suggest that such changes are minor (Stavrakou et al., 2020). Recent TROPOMI-based estimates show that a typical lifetime in urban areas is between 2 and 5 hours in spring and autumn with shorter lifetimes at low latitudes (Lange et al., 2021). While the lifetime has a large impact on the emission estimates, relative changes are less sensitive to it. The impact of the plume widths and lifetime parameters on the estimates and standard deviation of the residuals is discussed in the Supplement A.

Unlike many previous studies (Beirle et al., 2011; Fioletov et al., 2016; Lange et al., 2021) where the background offset was presumed to be constant and estimated from, for example, upwind NO_2 data, we included a special term that is

https://doi.org/10.5194/acp-2021-536
Preprint. Discussion started: 6 July 2021

Atmospheric Chemistry and Physics Discussions

responsible for it. In equation (1), the $\alpha_0 + (\beta_0 + \beta_1(\theta - \theta_0) + \beta_2(\varphi - \varphi_0)) \cdot exp(-H/H_0)$ term represents the "background" NO_2 that is assumed to be declining exponentially with elevation, i.e., within the analyzed 3° by 4° area, the higher is the elevation the lower is tropospheric column NO_2. It was also assumed that this contribution from elevation depends on geographical coordinates only and not on the winds. Even in absence of any sources, there could be some gradient in tropospheric NO_2 over the analyzed area, as for example, over some regions in northern Canada or along the east coast of the U.S. (Fig. 1). To account for such gradients, the linear term $\beta_1(\theta-\theta_0)+\beta_2(\varphi-\varphi_0)$, where θ_0 and φ_0 are the coordinates of the centre of the analyzed area, was added. In other words, it was assumed that there is a linear gradient of background NO_2 within the analyzed area and NO_2 VCD declines exponentially with height over elevated regions. Finally, α_0 was added to the model to account for remaining free-tropospheric NO_2 at high elevations where $exp(-H/H_0)$ is very close to 0. Its presence gives a better agreement with the satellite data for areas with a high range of elevations. Since this term is a part of the statistical model, all parameters α_0, β_0, β_1, and β_2 are estimated from the fitting. Once they are estimated, the term can be calculated for each location within the analysed 3°×4° area that gives a "background" value for that location that depends on the coordinates and elevation only. For simplicity, we will refer to the term discussed in this paragraph as to the "background" component.

The $a_p\,\Omega_p$ term represents the emissions contribution from factors, related to human activity, where the population density is used as a proxy. The population density data were converted to a 0.2° by 0.2° grid and then each of 336 (16 x 21) grid cells were considered as point sources located at the grid centre with emissions proportional to the population. However, instead of estimating emission for each such "source" separately, the emissions were parameterized by a single unknown parameter α_p. This means that emissions per capita are assumed to be the same everywhere within the analysed 3° by 4° area. The composite plume function Ω_p is, therefore, a sum of plume functions of all individual 0.2° by 0.2° grid cell centres multiplied by the grid cell population. Thus, Ω_p depends on geographical coordinates, population density and local winds.

Eq.1 is a linear regression statistical model with unknown coefficient sets α and β. The proxy functions used in the model preferably should be uncorrelated, because otherwise the coefficients have correlated errors making their interpretation difficult. There are three main components in the model: related to background and elevation (four fitted coefficients), to the population density (one coefficient) and to industrial sources (variable number of coefficients from zero to few dozens). We will refer to them as to background, urban and industrial components. For a typical urban area, these components should be independent: high population density zones typically occupy a small part of the area and industrial sources are typically located away from such highly populated zones. Note that the lifetime is relatively short (3.3 hours) and the median wind speed in, for example, the eastern U.S. is about 10 km per hour, so sources located 30-40 km apart typically have uncorrelated plume functions.

High correlation between the population and landscape-related proxies is possible if a city is in a valley surrounded by high mountains. The correlation could be reduced by increasing the size of the analysed area, but if the area is too large, the assumption that the background level has a linear gradient in the area may not be valid. Therefore, we limited the area to 3° by 4°. The correlation coefficients between the site elevation and population density for 3° by 4° areas are typically small. For example, in the U.S., correlations are positive over Florida (about 0.2) with the population density higher in the area above

https://doi.org/10.5194/acp-2021-536
Preprint. Discussion started: 6 July 2021


Atmospheric Chemistry and Physics Discussions

sea level, and negative in the Portland-Seattle-Vancouver area (about -0.35), where it is higher near the ocean and lower in the mountains. As the plume functions of individual industrial sources are very local (~50 km footprint), they do not correlate with the elevation. With such low correlation coefficients, elevation does not affect estimates of other parameters of the regression model.

When industrial point sources are located in close proximity, their plume functions in the statistical model (Eq.1) are highly correlated. In practice, it often appears as if, for example, estimated emissions from one source are unrealistically high, while emissions from the other near-by source are low or even negative. In such cases, emissions from individual industrial sources often cannot be estimated. However, the sources can be grouped into independent clusters and total emission from such clusters can be estimated. Such grouping could be done manually on a case-by-case basis, but it would be subjective and very time consuming. Instead, we applied an algorithm based on factor analysis. We would like to emphasize, that the factor analysis, described in the next three paragraphs, was used to improve emission estimation for individual sources or cluster of sources. It is not required if only total emissions from all point sources in the area are estimated in order to separate them from urban emissions or if all industrial sources are isolated remote sources.

To group industrial sources into clusters, an orthogonalization process was applied to the plume function of individual industrial sources. First, the correlation matrix for the plume functions of individual point sources (Ω_i) was calculated and eigenvalues and eigenvectors (or "factors") of the correlation matrix were determined. The correlation matrix was calculated just once using March 16 – June 15 data from all three years. An isolated remote source would appear as an eigenvector with an eigenvalue of 1. Two (or more) closely located, but isolated from others, sources, would have one corresponding eigenvector and an eigenvalue of 2 (or more). Eigenvalues lower than 1 mean that the corresponding sources are already partially included in other eigenvectors. To reduce the number of "factors", only "factors" with eigenvalues > 0.6 were kept.

The approach based on eigenvalues of the correlation matrix creates proxies that are not correlated and reduces the number of the fitting coefficients. While they correctly describe the total contribution of all industrial sources in the area in the total NO_2 variability (or total emissions), individual eigenvalues, i.e., linear combinations of the original plume functions, may not have clear interpretation. For example, they may include the original plume functions with negative coefficients. In order to avoid that and obtain proxies that have a meaningful interpretation, the eigenvalues were linearly transformed, so they became as close to the original plume functions as possible, while the correlation coefficients between them remained low.

This was done using the varimax factor analysis method that is implemented in modern statistical software packages such as R and SAS (Belhekar, 2013). It orthogonally rotates the established "factors" to maximize the sum of squared correlations between the original variables and factors. Then, the algorithm uses a linear combination of the original variables that have the highest correlations with the rotated "factors". I.e., the condition of orthogonality is removed in order to find the simplest linear combination of the original variables. In practice, the algorithm produces a set of "clusters", i.e., linear combinations of the original plume functions, that have low correlation coefficients (typically less than 0.2) between them, and each cluster has high correlation coefficient (typically more than 0.95) with one orthogonal "factor". To simplify this further, if a linear combination has a weight for an original variable under 0.2, its weight was set to 0. As a result, all non-

https://doi.org/10.5194/acp-2021-536
Preprint. Discussion started: 6 July 2021


Atmospheric Chemistry and Physics Discussions

isolated point sources were grouped into small clusters and emissions estimates were done for such clusters instead of individual sources, while each isolated remote source forms a single-source cluster that corresponds to only that source. It is possible that a single source contributes to more than one cluster that makes interpretation of emissions for such clusters more difficult, but such cases are rare.

As in any regression analysis-based study, correlation between the proxies is one of the main obstacles in the result interpretation. The "orthogonalization" of plume functions from industrial sources largely reduces cross-correlations between the proxies, but high correlations between industrial and population density-related plume functions are still possible if industrial sources are located in highly populated areas. In such cases, it may be difficult to separate its signal from the contribution of the population density-related proxy. For example, in one case (Edmonton, Canada) this correlation coefficient was as high as 0.94 and it was not possible to separate urban and industrial emissions there. For seven cities in the U.S. and Canada it was between 0.81 and 0.85 (for the remaining sources, it is less than 0.77). Note that for large cities and small industrial sources, high correlation means that the industrial emissions cannot be reliably estimated, although the impact on estimation of the population density-relate signal is small. We monitored the correlation coefficients between industrial and population density-related plume functions and, in some cases, excluded certain sources or even certain urban areas from the analysis.

The algorithm is illustrated in Fig. 2, where individual terms of Eq. 1 are shown for an area centred on Montreal. The area includes two large cities, Montreal (4.2 million) and Ottawa (1.4 million, including the sister city of Gatineau). The terrain elevations in the analysed area are in the range from just a few metres above sea level along the Saint Lawrence River to more than 500 meters 100 km north of Montreal. For this plot (as well as for Fig. 1 and other figures), we used a non-linear scale that is more sensitive to small quantities in order to make small deviations more pronounced. The top row of Fig. 2 shows the mean TROPOMI NO_2 data (Fig. 2a), the fitting results (Fig. 2b), and the difference between them or the residuals (Fig. 2c). Individual fitting components such as the background term ($\alpha_0 + (\beta_0 + \beta_1(\theta - \theta_0) + \beta_2(\varphi - \varphi_0))\cdot exp(-H/H_0)$), population density-related ($\alpha_p \Omega_p$) and industrial sources-related component are shown in Fig 2 panels d, e, and f respectively.

The contribution of industrial point sources ($\Sigma\ \alpha_i\Omega_i$) is illustrated by Fig. 2 g-i. The industrial source-related component itself contains contributions from three clusters of sources. In the case of Montreal, emissions from industrial sources are relatively small, less than 1.8 kt per year. Note that unlike the previous algorithm (Fioletov et al., 2017), where Ω_i represented plume functions from individual sources, this new Ω_i represents plume functions of clusters of closely located individual sources determined by factor analysis. The estimated parameter α_i represents emission from the entire cluster, while Ω_i is a weighted sum of plume functions of individual sources in the cluster. The weighting coefficients are determined by the varimax technique, described above. In the case of Fig. 2, the first cluster is comprised of two sources and the second and third clusters are each just single point sources. The total industrial point source component is a sum of all these clusters. Note that the varimax technique was applied to the correlation matrix based on plume functions and the weighting coefficients are determined by the source locations only and are not related to the emission strength of these sources. The estimated parameter α_i represents emission from the entire cluster, required that $\alpha_i \geq 0$ (although this condition has to be removed in several "extreme"

https://doi.org/10.5194/acp-2021-536
Preprint. Discussion started: 6 July 2021


Atmospheric Chemistry and Physics Discussions

cases of very high urban and industrial pollutions located in close proximity). Moreover, the emissions are estimated for the entire cluster only and cannot be estimated for individual sources within the cluster.

4 NO_2 VCDs over some urban areas

To test the method, the described technique was applied to the 22 largest urban areas in the U.S. and 5 in Canada. The analysis was performed on 3° by 4° (roughly, 330 km by 330 km areas at 40°N) areas for March 16-June 15, 2020 and for March 16-June 15, 2018-2019. It the latter case, estimates for each of the two years were averaged. The urban areas along with NO_2 maps for eight of them are shown in Fig. 3. The distributions are quite different in size and shape from area to area and the lockdown impact is not obvious from these maps, except for some large cities.

Four examples with detailed analysis of the components of the NO_2 distribution are discussed below with results shown in Fig. 4. Eight types of maps are shown. They include the actual TROPOMI data (column *a*), the fitting results (*b*), the residuals (*c*), i.e., (*a*) minus (*b*), as well as individual components of the fitting: the background (*d*), the urban (population density-related) (*e*), and the industrial source clusters (*f*). The residuals map can be used for detecting of missing in the inventory emission sources. "Hotspots" on the residual map (c) typically correspond to emission sources that are not included in the fitting. Coordinates of such sources are determined from high-resolution satellite imagery and added to the point source list and then the fitting process is repeated.

The suggested algorithm essentially finds the emission levels that give the best agreement with the TROPOMI data and then uses these estimates to "reconstruct" the spatial NO_2 distribution as well as contribution from each source. As explained by (Fioletov et al., 2017), the technique of VCD reconstruction from fitted coefficients α_i using Eq.1 used to isolate different components, can be applied to the reported emissions E_i. by using $\alpha_i = E_i \times \tau$. This produces a map of VCD that would be seen by satellites if these reported emissions are the only sources of NO_2. The same approach was employed here. In the U.S., directly measured industrial NO_x emissions from point sources are available. It was assumed that the NO_2 to NO_x ratio is constant 0.7. The map of NO_2 from the reported emissions is shown in Fig. 4 column (g). We would like to emphasise that such reconstruction is based on emissions data only, without any satellite NO_2 observations (although τ and w in the plume functions were the same as in the satellite-based estimates). Finally, the maps of the difference between industrial sources-related component and NO_2 from reported emission-based reconstruction is also shown (column h).

4.1 Case studies

In the case of Boston, there is a single urban source with no large industrial sources nearby and with relatively small impact from the terrain. The Atlanta area represents the case where the urban component is well-separated from industrial sources. In the Pittsburgh area, industrial and urban sources have comparable contributions, and the industrial emissions estimates can be validated by measured emissions. Multiple industrial sources in the Huston area are missing from the used EPA NEI emission

https://doi.org/10.5194/acp-2021-536
Preprint. Discussion started: 6 July 2021


Atmospheric Chemistry and Physics Discussions

database and this example illustrates why it was necessary to add locations of additional sources to explain the observed NO_2 distribution in the area.

Boston is a major urban area with a population of more than 8 million (for the Combined statistical area of Greater Boston). On the TROPOMI NO_2 map (Fig,4, col. *a*), it appears as a large "hotspot" that can be successfully reproduced by the statistical model (Eq.1) using the population density as a proxy. There is a 25% decline in the urban emissions in 2020 compared to the 2018-2019 average. It also shows one of the largest in the U.S. declines in the background component (about 15%).

The Atlanta area hosts the Hartsfield–Jackson Atlanta International Airport, the world's busiest with more than 100 million passengers per year in 2018-2019 (https://aci.aero/data-centre/annual-traffic-data/passengers/2017-passenger-summary-annual-traffic-data/). The Atlanta airport NO_2 signal can be easily isolated since the airport is located far away from industrial sources (the correlation coefficients between the plume functions are less than 0.2) and on a distance from Atlanta city's most populated area (the correlation coefficient is 0.54). VCDs estimated for the industrial source clusters (column *f* in Fig.4) are in line with those based on reported emissions (column *g* in Fig.4). When examining their difference (column *h*), the airport appears as a hotspot as its emissions are not included in the reported emissions inventory. All industrial sources (power plants) are also far away from the populated area and signals from these sources can be clearly separated from the population density-related signal. The area is flat, and the background level does not change very much within the area except for mountains to the north.

The Pittsburgh area has one of the highest emissions from industrial sources among all analysed areas in the U.S. Several coal-burning power plants are located east, west, and south of the city. The emissions from them are comparable or even larger than from the city itself. As mentioned, the NO_2 distribution around major industrial sources can be "reconstructed" from the emissions, reported by these sources (column *g* in Fig.4). The main features of the reconstructed NO_2 distribution from industrial sources based on satellite estimates, the reported emissions are rather similar, and the differences (column *f* minus column *g*) are small, although NO_2 from reported emissions are slightly larger for the cluster of power plans east of the city. The background values are fairly constant within the area except for the Appalachian Mountains area.

In the case of Houston, the EPA NEI emissions inventory contains emissions from the power plants in the area, but not from large oil refineries that are responsible for hotspots seen on the TROPOMI mean NO_2 plot. In order to reduce the residuals, we added the coordinates of 10 known refineries as industrial sources in Eq. 1. As a result, the residuals became small, although some elevated NO_2 values can still be seen in the industrial areas suggesting the list of refineries included in this analysis may not be complete. This example illustrates that it is necessary to add some sources to the list of sources based on the used EPA inventory, derived from measured emissions. A total of 56 sources across the US and Canada were added and the list of sources in the Supplement (file Additional_Sources_Canada_US.xls).

Landscape elevation plays an important role in the NO_2 distribution that can be illustrated by the following examples (Fig. 5). If the surface is nearly flat in the analysed area (as, for example, in the case of Minneapolis), the background component is dominated by a linear gradient. However, the elevation affects the NO_2 distribution near mountain areas as, for

https://doi.org/10.5194/acp-2021-536
Preprint. Discussion started: 6 July 2021

Atmospheric Chemistry and Physics Discussions

example, in case of Seattle where mountains as high as 2000 m are located east of the city. It is interesting to note that the background components are practically identical for both periods that gives a high confidence in the obtained results. The influence of the landscape on the NO_2 distribution also explains why the distribution near Seattle does not look like a "hotspot" NO_2 distribution near a typical large urban area.

4.2 Relative contribution of different components

NO_2 VCD represents total number of molecules, and equivalently mass, per area unit. When individual components affecting the NO_2 distribution are known, it is possible to estimate their relative contribution to the total mass based on Eq.1. The diagram in Fig. 6 shows such contribution of individual components for the Montreal area. Most NO_2 mass is associated with the term related to the background component. For the Montreal area, the contribution of industrial sources is four times less than the contribution of the urban component and the two of these components are responsible for less than a quarter of the total NO_2 mass in the area.

The mean NO_2 distribution near major emission sources has sharp gradients and estimates of the NO_2 lifetime from satellite data suggest that this time is relatively short, on the order of a few hours (Beirle et al., 2011; de Foy et al., 2015). It is even shorter than for satellite SO_2 VCDs (Fioletov et al., 2015). However, large background component may suggest that the lifetime should be relatively long since NO_2 distribution follows the terrain over large areas. This difference in the lifetime could be reconciled if we assume that a fraction of NO_2 emitted from cities and industrial sources gets into free troposphere and have a longer lifetime there than near the ground. Also, levels of the OH radical, the main chemical NO_x sink, within a plume can be much larger than under "clean" conditions and NO_2 lifetime could be longer under such condition than in the plume (~~Junceosa~~ Calahorrano et al., 2021). Other sources, e.g., lightning or soil emissions may contribute to background component NO_2 directly. The background term can also include components of stratospheric NO_2 that was imperfectly removed as part of the retrieval algorithm.

Relative contribution of the three components for the 2018-2019 period are shown in Fig, 7. Plumes from urban and industrial sources, or to be precise, $\alpha_p \Omega_p$ and $\Sigma \alpha_i \Omega_i$ terms in Eq.1, are responsible for less than a third of total NO_2 mass in all of the analysed 3° by 4° urban areas in the U.S and Canada. Most of NO_2 mass belongs to the background component that is not directly linked to particular urban or industrial sources. Fig. 7 also shows that NO_2 mass emitted from cities are larger than emissions from the industrial sources for most of analysed areas in the U.S. and Canada.

4.3 The COVID-19 lockdown impact: the U.S. and Canada

The ability of the method to isolate individual components of the total NO_2 mass makes it possible to estimate the impact of the COVID-19-related lockdown on these components. The results for the background, urban, and industrial components are shown in Fig. 8. As mentioned, we compared the averages for the period from March 16 to June 15 in 2018 and 2019 to the same period averages for 2020.

https://doi.org/10.5194/acp-2021-536
Preprint. Discussion started: 6 July 2021


Atmospheric Chemistry and Physics Discussions

To illustrate the changes in the background component, Fig. 8 (top) shows the mean VCD values of that component shown in Fig 4, column *d* (or, in other words, the mean value of $\alpha_0 + (\beta_0 + \beta_1(\theta - \theta_0) + \beta_2(\varphi - \varphi_0))\cdot exp(-H/H_0)$) for the analyzed areas for the two time intervals (left) as well as the percentage change in 2020 vs. 2018-2019 values (right). The mean value of decline for the background components among all urban areas is -1.0% ± 3.3% (all error bars in the study correspond to 2σ-level). Thus, the average background value in 2020 was almost the same as in 2018-2019.

The changes in the urban component are shown in Fig. 8 (middle) expressed as NO_2 emissions per capita. Recall, that emission rate is the mass divided by the lifetime (that was assumed constant for all areas), therefore, the changes in emissions per capita and the changes in total mass are identical. The relative changes for the urban component (Fig. 8 right) are typically larger than those for the background component. The average total emissions per capita declined by -28% in 2020 compared to 2018-2019 average (from 5.6 to 4 kg per capita per year). The median value of decline among all urban areas is -32% and the mean value of percentage decline is -26% ± 5.6%. The changes in emissions per capita are rather uniform except Vancouver where 2020 emissions are 15% larger than the average 2018-2019 emissions. The reason for that is not immediately clear but may be related to unusual meteorology and persistent cloud cover there in 2020. Information about statistical significance of such "outlier" can be obtain from estimates of interannual variability based on 2018 and 2019 data. The variance of the difference between 2018 and 2019 mean values is equal to the variance of the mean NO_2 value multiplied by two. While two years from one area is not enough to estimate the variance, the variance can be reliably estimated if we assume that the interannual variability is the same for all analysed areas (See Supplement A). This gives us the error bars for the Vancouver 2020 value: 15%±19.5%, i.e., this value is within the natural variability range. Edmonton was excluded from this analysis because the plume functions from two industrial sources are highly correlated to the population density-related plume function (see section 3) and, therefore, it is hard to separate emission from them. Without such separation, industrial emissions are counted as population density-related that makes Edmonton per capita emissions nearly twice larger than emissions for other cities (see Supplement B).

The number of sources and emission strength from large industrial sources varies with the urban area. Some areas, e.g., Las Vegas, do not have such emissions sources at all. The total emission from all large emission sources and percentage change in emissions are shown in Fig. 8 (bottom). The mean value of percentage decline in the areas with industrial sources is 28% ± 6%. Unlike background and urban components, changes in emissions from industrial point sources demonstrate rather large scattering from one area to another. It is not a surprise since different industrial sectors were affected by COVID-19 differently.

Since point source emission estimates are obtained as part of our TROPOMI NO_2 data analysis, such estimated emissions can be compared to the reported ones. In general, there is an overall agreement between estimated and reported emissions, as was already demonstrated in Fig. 4. The scatter plot of estimated vs. reported emissions in 2018-2019 is shown in Fig. 9 for the U.S. urban areas. For this analysis, in the fitting we used only point sources where reported emissions data were available. A constant lifetime of 3.3 hours was used, although the lifetime may be different from source to source as discussed in Supplement B. However, for total industrial source emissions calculated for urban areas, there is a good correlation

https://doi.org/10.5194/acp-2021-536
Preprint. Discussion started: 6 July 2021


Atmospheric Chemistry and Physics Discussions

with the reported emissions: the correlation coefficients between the two data sets from Fig. 9 is 0.9. Note that 2020 US EPA NEI reported emission were incomplete at the time of this study.

4.4 The COVID-19 lockdown impact: Europe

The described technique was applied to the European Union countries (plus non-members from former Yugoslavia) where detailed information about the industrial emissions sources is available. The analysis was also done for 3° by 4° areas around 36 largest European cities with population greater than 1 million plus some national capitals with population more than 500,000. At the time of this study, the 2020 emissions data were not available, and the 2018-2019 emissions inventory was incomplete with data from many countries missing. Unlike the U.S., the available data were only annual, not monthly, and emissions were typically estimates and not direct measurements. We used the 2017 inventory to obtain the coordinates of the largest sources and then use them in the fitting algorithm. Note, that to avoid double-counting, if more than one city located within an area, we used that area just once (e.g., Manchester and Birmingham are in one area).

The absolute and relative changes between 2018-2019 and 2020 for the three components are shown in Fig. 10. The NO_2 decline was particularly large, more than 50%, for the countries in the most western part of the continent where the strictest lockdown measures were taken: France, Spain, and UK. In contrast, the decline in the German, Czech and some other East European cities was only 20-25%. For this reason, two sub-regions were formed for the analysis: Europe-1 (Italy, France, Spain, Portugal, Belgium, Ireland, and UK) and Europe-2 with all other countries. In general, the mean background values and estimated NO_2 emissions rates per capita in Europe are similar to those in the U.S. and Canada. However, relative changes are somewhat different.

In 2018-2019, the estimated emissions per capita for both European regions were very similar to those for the U.S. and Canada. In 2020, the urban component declined in almost every analysed area. The average declines for Europe-1 and Europe-2 regions were -52% ±5% and -14% ±8% respectively. This is in general agreement with NO_x emission reduction for these two European sub-regions (Guevara et al., 2021). The decline in Europe-1 was rather uniform with all but one area demonstrating a decline of more than 40%. In contrast, only two areas demonstrated a 40% decline in Europe-2, while most of the areas had a decline under 20%. Two areas in Europe-2 (Budapest and Belgrade) demonstrated an increase in NO_2. They are located 320 km apart and it is possible that relatively high NO_2 values there were cause by some specific meteorological conditions in spring of 2020: the NASA GEOS Composition Forecasting (GEOS-CF) simulations show a positive NO_2 anomaly over Hungary in April-May 2020.

As in the case of the U.S. and Canada, the mean background component in Europe shows a smaller decline than the urban component. On average, it was -5%±2% and -12±3% lower in 2020 than in 2018-2019 for Europe-1 and Europe-2 regions respectively, but it was pretty consistent as almost all individual areas demonstrated a decline. Large decline in population-related emissions and relatively small decline in the background component for Europe-1 and the opposite for Europe-2 may create an impression that here is anticorrelation between the background level and population-related component, but it is not true. The large decline in average background for Europe-2 was caused by large negative background

https://doi.org/10.5194/acp-2021-536
Preprint. Discussion started: 6 July 2021


Atmospheric Chemistry and Physics Discussions

values for the Scandinavian countries in 2020 that also had large negative changes in the urban components. As discussed later in Section 4.5, there is no correlation between the background levels and urban component.

The emissions from industrial sources also demonstrated a decline, although the scattering of the values is large as the changes varies from country to country and from sector to sector. The average decline value is -34%±10 and -13%±16% for Europe-1 and Europe-2 regions, respectively.

For illustration purpose, four areas are examined in greater detail below. The Manchester-Birmingham plot (Fig. 11) illustrates a large area of high population density with several power plants to the East. The TROPOMI data analysis shows a 40% decline in the population density-related component and about 25% decline from total emission from the power plants. In contrast, the background component shows almost no change in 2020 compared to 2018-2019.

Paris is an example of a city that appears as a large, isolated urban source. The decline in the population-related signal is about 55% and can be clearly seen on the plot. The only relatively large point source in the Paris area is Charles de Gaulle Airport that is evident on the 2018-2019 plot and practically disappeared on the 2020 plot. The terrain does not play a major role in background component of the Paris area. There is some north-south gradient in the background component with higher values at the north-eastern corner of the area. The change between the two periods in background mean values is only about 5%.

Complex terrain affects the NO_2 distribution creating large differences between VCD values over the mountains in valleys in the Milan area. The urban component demonstrates a more than 50% decline in 2020, while the background component shows practically no difference between the two periods. Complex terrain also makes it more difficult to fit the observations with the plume functions based on assumption of straight-line plumes resulting in relatively high residuals. The contribution from industrial point sources for that area is very small.

The plots for the Prague area illustrate how changes in NO_2 from industrial sources reflect differences in COVID-19 policies in Germany and Czech Republic. The decline in the urban component was only about 20%. In addition to Prague, that component also includes cities in East Germany (Dresden, Leipzig), but it appears that the changes over these cities and Prague are similar. Otherwise, the difference would appear in the residuals (Fig. 10, column *c*). The main industrial sources in the Prague area are coal mines and coal-burning power plants in Czech Republic west of Prague near the German border and in Germany north of Prague, near the Polish border. In Czech Republic, the NO_2 values of the industrial component remain unchanged, while the values over German industrial sources declined by a factor of 2. This is likely the result of different approaches to coal power industry in two countries. In the Czech case, power plants remained fully functioning and certain steps were taken to assure smooth operation and protect the workers: employees of power plants stayed on their job for longer periods, to avoid the risk of infection at home (EC, 2020). In Germany, with its focus on renewable energy sources, a different approach was taken. The power generation from coal-burning plants was reduced by 60% (from 13.4 TWh to 5.6 TWh per month) in April-May 2020 compared to 2019 (https://www.energy-charts.info/charts/energy/chart.htm?l=en&c=DE&year=2020 accessed on March 1, 2021), while production from renewable energy sources was increased. As a result, we see a large difference in NO_2 changes from the power plants in two countries.

https://doi.org/10.5194/acp-2021-536
Preprint. Discussion started: 6 July 2021

Atmospheric Chemistry and Physics Discussions

4.5 The global COVID-19 lockdown impact

To evaluate the COVID-19 lockdown impact worldwide, the analysis described earlier in Section 4 was performed for 263 urban areas around the world. It should be noted that the NO_2 "footprints" of cities with the same population vary greatly from region to region with the highest values in Northern Eurasia and Australia, and the smallest in Africa and India. To illustrate these large differences, Fig. 12 shows the examples of NO_2 distribution near cities with population of about 5-6 million with very large (Saint Petersburg, Russia) and very small (Dar es Salaam, Tanzania) per capita emissions. The total mass of NO_2 per capita related to the urban component for Saint Petersburg was 40 times larger than for Dar es Salaam (all for 2018-2019). While all cities with population greater than 1 million were considered in this study, some of them do not even produce significant NO_2 emissions that can be measured by TROPOMI over the three-month period selected for this study. Another obstacle is in Western Africa, where biomass burning made it difficult to estimate "background" levels as they were very different from year to year. In case of China, there are too many cities with population over one million. We raised the limit and considered only cities with population greater than 6 million to keep the number of analysed areas similar to other regions.

The analysis algorithm requires coordinates of individual industrial sources in order to separate them from the urban component. Detailed information about industrial source locations is often not available in many regions. The world power plant database (see section 2.3) was used to locate most of the power plants, while other sources were identified from hotspots on the NO_2 maps. A total of 357 such additional sources were identified. Most of them were cement and steel factories, and oil refineries. The complete list of these additional sources is included in the Supplement (file Additional_Sources_World.xls). In addition, the world busiest airports were included as "industrial" emission sources. However, some sources, in particular, ship tracks may still be missing that may affect estimates for some areas. An example is given in Supplement D. Also, the main highways are not included in the present statistical model. Some of them are identifiable in the residual maps. Ship tracks and highways could be added to the statistical model in the future.

The map of mean background component values for all 263 sites is shown in Fig. 13 (top). The analysed period from mid-March to mid-June is close to spring in the Northern Hemisphere and autumn in the Southern Hemisphere, i.e. the seasons with very similar values of lifetime (Lange et al., 2021). Therefore, seasonal differences between the two hemispheres should be minimal, and maps of the main estimated components should well represent their global distribution. The highest values are seen over East China and the northern part of Central Europe, while the lowest are mostly over South America and East Africa. In general, it is similar to the global NO_2 distribution (Krotkov et al., 2016), although the background levels are much lower than those seen over NO_2 hotspots on the mean satellite NO_2 map.

The values of the urban component, expressed as annual emission rate per capita, are shown in Fig. 13 (bottom). The highest values are over Russia and are likely related to additional NOx emissions due to heating in a relatively cold period in March-April. Another hotspot is Edmonton, but as mentioned, its high value is due to poor separation urban emissions from emissions from two industrial sources there. Emissions per capita are also high over Middle East. The lowest emissions per

https://doi.org/10.5194/acp-2021-536
Preprint. Discussion started: 6 July 2021


Atmospheric Chemistry and Physics Discussions

capita are in South America, Africa, and India. Although emissions per capita were calculated for each area independently and the population and industrial sources vary greatly from area to area, the per capita values are uniform: for example, all areas in India marked by green dots, most of European areas are orange, etc. This further gives a confidence in the obtained estimates.

The estimates for individual areas were then grouped into 13 large regions with 10-20 areas in each: the U.S. and Canada, Europe-1 and -2, China, India, South-East Asia (includes also Pakistan and Bangladesh), Japan (with Taiwan and South Korea), Northern Eurasia (former USSR countries and Mongolia), Middle East, Africa, Australia and New Zealand, Central America, and South America. The regions are based on geographical location with similarities in economic development and reactions to the COVID-19 pandemic were also taken into account. Then, the average characteristics of the background, urban and industrial components were calculated for each region. Relative contributions of the three components (similar to Fig.7) and the bar charts of the mean values of these components as well as the decline between 2020 and 2018-2019 for all regions are available from the Supplement. Three areas, Johannesburg (South Africa), Nicosia (Cyprus), and Pyongyang (North Korea) were not included in any region.

The summary results for the regions are shown in Fig. 14, while the results for individual areas within each region as well as the obtained emissions values are available from the Supplement. The regions in Fig. 14 are sorted by relative decline in the urban component (from smallest to largest). The regional changes were calculated as the average of percent changes for individual areas for that region and areas with components below some threshold levels were excluded. Fig. 15 shows the maps of changes for individual areas for the background and urban components.

China shows the smallest and not significant decline in the urban component, while the majority of the regions demonstrated statistically significant urban emissions decline within the range 18-28%. The decline was the largest, 36-52%, in three regions: Europe-1, South America and India. The map of the urban emission changes (Fig.15, bottom) shows that the first two regions indeed contain countries with large decline of urban emissions. In case of India, a similar decline can be seen in neighbouring Pakistan and Bangladesh. In Africa, a decline is seen at the south and the north of the continent, while countries in West Africa mostly show no decline and even some increase probably due to a contribution from forest fires.

Changes in the background component are shown in Fig. 14 and Fig. 15 (top). Relative changes of the background component are typically within ±10% and much smaller than in the urban component. One of the exceptions is the Scandinavian countries and Germany that caused an overall -13% change in the background value for the Europe-2 region. The urban and background components are fairly independent. Analysis of all 263 areas revealed that there is no correlation between changes in urban NO_2 emissions and changes in background values (the correlation coefficient is -0.009).

As mentioned in section 4.3, the industrial NO_2 component varies from area to area and from one type of NO_2 source to another, although there are some clear regional differences. As the main COVID-19 lockdown in China occurred earlier (in February), during the analysed period, Chinese cities demonstrated the smallest changes in both urban and industrial components (-2.8% and +5% respectively). There is, however, one exception. Emissions from Wuhan, the city where the pandemic begun, declined by more than 60%. Industrial emissions also declined, but only by 30%. The background component shows no change there. A very strict Wuhan lockdown ended on April 8, 2020, but during that lockdown, NO_2 emissions in

https://doi.org/10.5194/acp-2021-536
Preprint. Discussion started: 6 July 2021


Atmospheric Chemistry and Physics Discussions

Wuhan declined 82% relative to the 2019 level (Ghahremanloo et al., 2021). That strict lockdown period lasted for less than one third of the analysed period, but apparently, it took some time for NO_2 emissions to return to the pre-lockdown levels.

The largest industrial emissions decline was observed over the same regions where the largest urban emissions decline was observed: Europe-1 and India. It is likely the severe restrictions during the COVID-19 lockdown period there affected the industrial activity. However, on a larger scale this link is not that obvious. Although the lockdown had impact on industrial sources, the correlation coefficient between changes urban and industrial emissions among all analysed areas is only 0.18.

The uncertainties values in Fig. 14 for the regions are based on variation of the values for individual areas within the region. The uncertainties for individual area emissions can be estimated from the differences between 2018 and 2019 values as discussed in Supplement A (see also Table S1). The background component has the smallest variability among the three components typically between 5% and 9%. The urban component variability is between 7% and 17% and the decline observed in the urban component for South America, Europe-1 and India is outside 3-σ limits even for individual areas in these regions. The industrial component was largely added to separate emission from large industrial sources in the urban areas from urban emissions themselves. Emission from such industrial sources are typically similar or smaller than urban emissions and the variability of the industrial component (10%-30%) is similar or larger than that for the urban component.

To demonstrate that the observed NO_2 changes in urban emissions are indeed linked to the restricting measures taken by different countries, the estimated percent NO_2 changes in emissions per capita were compared to the Google Each Community Mobility Report data (available from https://www.google.com/covid19/mobility/, accessed on March 1, 2021). The mobility data represent the changes in the number of people at locations of various type and can be used as a proxy for the urban traffic. The three components of NO_2 distribution were compared various characteristics of mobility data. The mean values of the three components of the NO_2 distribution (background, urban, and industrial) were calculated for every country by averaging the corresponding values for individual cities. Only countries with two or more cities were used in the comparison. Similarly, the mean characteristics of mobility were calculated for all individual countries. Note that the mobility data were averages of all regions for the entire country, while the NO_2 changes were estimated for areas around large cities only. Mobility data for China, Korea and some other countries were not available.

The scatter plot of the mobility and the lockdown-related NO_2 changes (Fig. 16) demonstrates a very different relationship between mobility changes and changes in urban and background components. Changes in mobility and urban components are correlated (Fig. 16 left). As expected, the relative changes in the urban component are smaller than the mobility changes as the urban component includes more than just mobility-related traffic. The highest correlation is observed when changes in the NO_2 urban component are compared with mobility for "retail and recreation", covering visits to restaurants, cafes, shopping centers, theme parks, museums, libraries, movie theatres, and similar locations. The correlation coefficient between the percent changes in per capita emissions and "retail and recreation" mobility is 0.66 (the probability that there is no correlation is less than 0.0001). The correlations of the urban component with other mobility characteristics are lower (about 0.55 and 0.58 for the "workplaces" and "transit stations" categories, respectively). In contrast, there is no statistically significant correlation (the correlation coefficient is 0.03) between the background NO_2 and mobility data (Fig. 16 right). The

https://doi.org/10.5194/acp-2021-536
Preprint. Discussion started: 6 July 2021


Atmospheric Chemistry and Physics Discussions

industrial component shows some correlation (the correlation coefficient is 0.5) with the mobility data, although not as high as for the urban component.

To compare our results with other similar estimates of NO_x emission, we looked at a recent study by Lange et al., 2021. In their study, TROPOMI NO_2 data were used to estimate emissions from 45 sources worldwide and compared them with the available emissions inventories and some other satellite-based emission estimates. As our study also provides total emissions estimates (the sum of urban and industrial emissions) for 33 of them, we compare our results with those from Lange et al., 2021. While the emission estimation algorithms and approaches are different in the two studies, the results show a good agreement and the correlation coefficient between the two sets of emission estimates is 0.78. As expected, the emission estimated in this study are higher than from Lange et al., 2021. This is because we used larger areas and, typically, there was more than one emission source in the analysed 3° by 4° areas of this study. The details of this comparison are available from Supplement C.

In this study, the population density was used as a proxy for urban emissions. We found that this proxy works well unless the population density was very high and the link between population density and emissions might not be linear anymore. Such exceptions were rare (e.g., some regions of New York City). To test the impact of such nonlinearity, we used a different proxy, the night light data set and all calculations were repeated with them. Unlike the population density, the used night light data reached saturation at highly populated areas and did not grow any further. It was found that the results were similar and the major findings about different reaction of the background and urban components to the COVID-19 lockdown were still valid, although with some differences in absolute values (see section Supplement E). The correlation coefficient between mobility and urban emissions estimated from night light is lower (0.57) that for those from population density suggesting that the population density-based analysis captures the NO_2 emissions reduction due to lower traffic better.

5 Discussion and conclusion

Statistical regression analysis was used to separate contribution from industrial sources, urban areas, and background levels to the observed tropospheric NO_2 VCD and to study the impact of the COVID-19 lockdown on each component separately. The analysis was done for 263 major urban areas around the world grouped into 13 large regions. The algorithm essentially estimates the total NO_2 mass for the three different components that then can be converted to emissions assuming a constant NO_2 lifetime (or, more accurately, decay time). A constant value of 3.3 hours was used as the lifetime.

Unlike other similar studies that simply removed the background offset (e.g., (Beirle et al., 2011; Lange et al., 2021)), this study included the background component in the analysis. On a scale of several hundred km (as we analyzed 3° by 4° areas), most of the NO_2 mass is typically related to the background component. Even in the areas such as New York City, the background component accounts for 2/3 of the total mass. This explains why the estimated impact of the COVID-19 lockdown in urban areas depends on the size of the analysed area: the bigger the size the more background NO_2 it includes and, therefore, the smaller is the NO_2 difference between the COVID-19 lockdown and reference periods.

https://doi.org/10.5194/acp-2021-536
Preprint. Discussion started: 6 July 2021


Atmospheric Chemistry and Physics Discussions

In most of the analysed areas, changes in the background components between the COVID-19 lockdown period analysed here (from March 16 to June 15, 2020) were typically within 10% from the 2018-2019 levels. In contrast, the urban component, based on population density, demonstrated a substantial and rather uniform decline of about 20%-30% in most of the regions. Three regions (most western part of Europe, India and South America) demonstrated a larger decline, about 40%-50%. China showed a much smaller decline (-3%±9%) because the lockdown there occurred prior to the analysed period. As for industrial point sources, emissions from them varied from region to region and from sector to sector. On average, they demonstrate an about 20% decline.

Abrupt changes and urban and industrial emissions due to COVID-19 lockdown did not immediately result in a similar decline in the background component. This may explain why large changes in NO_2 emissions in urban areas produced a relatively small, about 9% decline in global NO_2 (Bray et al., 2021). The importance of background NO_2 VCD was previously noted by Qu et al., (2021) and Silvern et al., (2019) when they found that the observed satellite trends in remote areas do not match the expected changes. The background NO_2 is anticorrelated with the surface elevation. There are several possible factors that contribute to the background component. It could be related to NO_2 in the free troposphere where it may have a much longer lifetime and travel long distances. Satellite measurements are also more sensitive to NO_2 in the free troposphere than in the boundary layer and a relatively small amounts of NO_2 there produce a larger signal in satellite data. Another possible explanation is that at low concentration in the boundary layer, NO_2 may have longer lifetimes than the value of several hours in the plumes. The fact that NO_2 fluctuations remain persistent over longer time in clean conditions than over polluted conditions (Vinnikov et al., 2017) indirectly confirms that.

The origins of background NO_2 are still largely related to urban and industrial sources as it is clearly higher in the northern hemisphere, particularly over China, Central Europe and Eastern U.S., than in the southern hemisphere and tropics. However, the analysed three-month period may simply be not long enough for the lockdown to cause large changes in the background levels. There are also other NO_x sources such as soil emissions (Hudman et al., 2012; Sha et al., 2021). They as well as sources aloft, such as lightning, and to a lesser extent, aircraft NO_x directly contribute to the background component. It is estimated that lightning is responsible for roughly 16% of global production and most of this NO_x is found in the free troposphere (Bucsela et al., 2019).

The urban and industrial components are based on plume dispersion functions and correspond to NO_2 near the ground, probably in the boundary layer. The urban component is based on the population density and the assumption that emissions per capita are uniform everywhere in the analysed area. There are very large differences, up to factor of 40, in estimated emissions per capita between the areas. The estimates were done for 3-month periods. For such short time interval, most of the cities with population more than 1 million produce a statistically significant signal, that can be detected in TROPOMI NO_2 data. As estimated emissions per capita are rather uniform, they can be used to account for urban component outside large cities. Thus, it should be possible to estimate background, urban, and industrial components on the global scale and analyse the residuals in search of other factors contributing to the NO_2 budget.

https://doi.org/10.5194/acp-2021-536
Preprint. Discussion started: 6 July 2021

Atmospheric Chemistry and Physics Discussions

The approach described in this study can be used to estimate emissions from cities and industrial point sources. For the latter, only source coordinates are required. A comparison of reported and derived from TROPOMI data NO_2 emissions for the U.S. demonstrated a good correlation (0.9) between them. As source coordinates can be also detected from satellite data alone (Beirle et al., 2019; Ding et al., 2020; McLinden et al., 2016), it may be possible to develop an independent "top-down" NO_2 emission inventory from satellite measurements to complement and emissions improve available "bottom-up" inventories as it was done for SO_2 (Liu et al., 2018). This could be important for regions, where no other emission information is available.

Data availability

The TROPOMI NO_2 product is publicly available on the Copernicus Sentinel-5P data hub (https://s5phub.copernicus.eu).

Author contributions

VF analysed the data and prepared the paper with input from CM and critical feedback from all the co-authors. CM and DG generated the TROPOMI data subsets for the analysis. NK and FL contributed to the interpretation of the results. HE provided the TROPOMI NO_2 data product and related information. All authors read and agreed on the published version of the paper.

Competing interests

The authors declare that they have no conflict of interest.

Acknowledgments. Sentinel 5 Precursor TROPOMI Level 2 product is developed with funding from the Netherlands Space Office (NSO) and processed with funding from the European Space Agency (ESA). We thank Shailesh Kharol for assistance with night light data.

https://doi.org/10.5194/acp-2021-536
Preprint. Discussion started: 6 July 2021

Atmospheric Chemistry and Physics Discussions

Appendix

This appendix contains additional details of the used fitting algorithm that is largely based on the algorithm for multiple point source emission estimates (Fioletov et al., 2017). TROPOMI NO_2 VCD can be expressed as a sum of contributions $\alpha_i \cdot \Omega_i$ from all individual industrial sources (i), a population density-related term $\alpha_p \Omega_p$, an elevation-related background, and noise (ε):

$$TROPOMI\ NO_2(\theta, \varphi) = \alpha_0 + \alpha_p \Omega_p(\theta, \varphi) + \Sigma\, \alpha_i \Omega_i(\theta, \varphi) + (\beta_0 + \beta_1(\theta - \theta_0) + \beta_2(\varphi - \varphi_0)) \cdot exp(-H(\theta, \varphi)/H_0) + \varepsilon(\theta, \varphi) \quad \text{(A1)}$$

All Ω function are normalized (i.e., their total integral equals to 1) plume functions: the value of that function for a particular pixel with latitude θ and longitude φ, is proportional to the value of the plume parameterization from the source i located at the latitude θ_i and longitude (φ_i) (all in radian). The parameterization assumes that the plume is moving downwind along a straight line has a Gaussian shape spread across that line. To describe the plume, we can rotate satellite pixels for a particular day around the source, so the plume would always be moving from north to south, apply the plume parameterization, and then rotate the pixels back. If (x_i, y_i) and (x'_i, y'_i) are the pixel's Cartesian coordinates (km) in the system with the origin at the source i before and after the rotation respectively, then they can be calculated from the pixel and source latitudes and longitudes as:

$$x_i = r \cdot (\varphi - \varphi_i) \cdot \cos(\theta_i);$$
$$y_i = r \cdot (\theta - \theta_i);$$
$$x'_i = x_i \cdot \cos(-\omega) + y_i \cdot \sin(-\omega);$$
$$y'_i = -x_i \cdot \sin(-\omega) + y_i \cdot \cos(-\omega);$$

where r=111.3 km·180/ π (or r=6371 km· π/180 for latitude and longitude in degrees); ω is the pixel wind direction (0 for north); φ_i and θ_i are the source i longitude and latitude (all in radian). Note that there was a typo in this original formula for r in Fioletov et al., (2017).

Following Fioletov et al., (2017), the contribution $\alpha_i \cdot \Omega_i = \alpha_i \Omega(\theta, \phi, \omega, s, \theta_i, \phi_i)$ from the source i can be expressed as $\alpha_i \cdot \Omega_i = \alpha_i \cdot f(x'_i, y'_i) \cdot g(y'_i, s)$, where:

$$f(x'_i, y'_i) = \frac{1}{\sigma_1 \sqrt{2\pi}} exp\left(-\frac{x'^2_i}{2\sigma_1^2}\right);$$
$$g(y'_i, s) = \frac{\lambda_1}{2} exp\left(\frac{\lambda_1(\lambda_1 \sigma^2 + 2y'_i)}{2}\right) \cdot erfc\left(\frac{\lambda_1 \sigma^2 + y'_i}{\sqrt{2}\sigma}\right);$$
$$\sigma_1 = \begin{cases} \sqrt{\sigma^2 - 1.5 y'_i}, y'_i < 0; \\ \sigma, y'_i \geq 0; \end{cases}$$
$$\lambda_1 = \lambda / s; \quad \text{(A2)}$$

It is assumed that NO_2 emitted from a point source decline exponentially (i.e., as $exp(-\lambda t)$) with time (t) with a constant "lifetime" (or decay rate) τ=1/λ. The second parameter is the plume width (σ).

https://doi.org/10.5194/acp-2021-536
Preprint. Discussion started: 6 July 2021

Atmospheric Chemistry and Physics Discussions

Note that $\int_{-\infty}^{\infty}\int_{-\infty}^{\infty} f(x,y)\cdot g(y,s)dxdy = \int_{-\infty}^{\infty}(\int_{-\infty}^{\infty} f(x,y)dx)\cdot g(y,s)dy = \int_{-\infty}^{\infty} g(y,s)dy = 1$, therefore the parameter α_i represents the total observed number of NO_2 molecules (or the NO_2 mass) near the source *i*. If *TROPOMI* NO_2 is in DU, and σ is in km, then *a* is in $2.69\cdot10^{26}$ molec. or 0.021 T(NO_2). Furthermore, the emission strength (*E*) can be calculated as $E = \alpha/\tau$ assuming a simple mass balance.

As mentioned in section 3, some of the sources used in the analysis are not point sources but clusters. In that case, $\Omega_i = \sum_j w_j \Omega_j(\theta, \phi, \omega, s, \theta_j, \phi_j)$, where Ω_j is the plume function for source *j* and w_j is the weighting coefficient established by the factor analysis.

Similarly, $\alpha_p\,\Omega_p$ represent the contribution from the population density-related component, where Ω_p is the plume function from an area-distributed source. Ω_p is a weighted sum of plume functions from a grid with the weighting coefficients proportional to the population of at the grid points $\Omega_p = \sum_{ij} \rho_{ij}\Omega(\theta, \phi, \omega, s, \theta_{ij}, \phi_{ij})$, where θ_{ij}, ϕ_{ij} are the grid points coordinates and ρ_{ij} is the population associated with that grid points. Thus, α_p is the coefficient that represent the total NO_2 mass the corresponds to one person. In our calculations we used 3° by 4° area with a 0.2° by 0.2° grid with 336 (16 x 21) grid cell.

Finally, the elevation-related background term $\alpha_0 + (\beta_0 + \beta_1(\theta - \theta_0) + \beta_2(\varphi - \varphi_0)) \cdot exp(-H/H_0)$, where θ_0 and φ_0 are the coordinates of the centre of the analyzed area and *E* is the elevation in km and H_0=1 km, is determined by three parameters.

Equation (A1) represents a linear regression model where the unknown parameters α_p, α_i can be estimated from the measured variable (*TROPOMI* NO_2) at many pixels and known regressors. The fitting was done three times using all data for the analysed period (March 16 – June 15) in 2018, 2019, and 2020.

https://doi.org/10.5194/acp-2021-536
Preprint. Discussion started: 6 July 2021

Atmospheric Chemistry and Physics Discussions

References

Bao, R. and Zhang, A.: Does lockdown reduce air pollution? Evidence from 44 cities in northern China, Sci. Total Environ., 731, doi:10.1016/j.scitotenv.2020.139052, 2020.

Bauwens, M., Compernolle, S., Stavrakou, T., Müller, J. F., van Gent, J., Eskes, H., Levelt, P. F., van der A, R., Veefkind, J. P., Vlietinck, J., Yu, H. and Zehner, C.: Impact of Coronavirus Outbreak on NO2 Pollution Assessed Using TROPOMI and OMI Observations, Geophys. Res. Lett., 47(11), 1–9, doi:10.1029/2020GL087978, 2020.

Beirle, S., Platt, U., von Glasow, R., Wenig, M. and Wagner, T.: Estimate of nitrogen oxide emissions from shipping by satellite remote sensing, Geophys. Res. Lett., 31(18), L18102, doi:10.1029/2004GL020312, 2004.

Beirle, S., Boersma, K. F., Platt, U., Lawrence, M. G. and Wagner, T.: Megacity emissions and lifetimes of nitrogen oxides probed from space, Science (80-.)., 333(6050), 1737–1739, doi:10.1126/science.1207824, 2011.

Beirle, S., Hörmann, C., Penning de Vries, M., Dörner, S., Kern, C. and Wagner, T.: Estimating the volcanic emission rate and atmospheric lifetime of SO2 from space: a case study for Kīlauea volcano, Hawai`i, Atmos. Chem. Phys., 14(16), 8309–8322, doi:10.5194/acp-14-8309-2014, 2014.

Beirle, S., Borger, C., Dörner, S., Li, A., Hu, Z., Liu, F., Wang, Y. and Wagner, T.: Pinpointing nitrogen oxide emissions from space, Sci. Adv., 5(11), doi:10.1126/sciadv.aax9800, 2019.

Belhekar, V. M.: Factor Analysis and Structural Equation Modeling, in A Step-by-Step Approach to Using SAS® for Factor Analysis and Structural Equation Modeling, Second Edition, edited by N. O'Rourke and L. Hatcher, pp. 314–361, SAS Institute., 2013.

Bray, C. D., Nahas, A., Battye, W. H. and Aneja, V. P.: Impact of lockdown during the COVID-19 outbreak on multi-scale air quality, Atmos. Environ., 254(August 2020), 118386, doi:10.1016/j.atmosenv.2021.118386, 2021.

Bucsela, E. J., Pickering, K. E., Allen, D. J., Holzworth, R. H. and Krotkov, N. A.: Midlatitude Lightning NOx Production Efficiency Inferred From OMI and WWLLN Data, J. Geophys. Res. Atmos., 124(23), 13475–13497, doi:10.1029/2019JD030561, 2019.

C3S: Copernicus Climate Change Service (C3S) : ERA5: Fifth generation of ECMWF atmospheric reanalyses of the global climate. Copernicus Climate Change Service Climate Data Store (CDS), [online] Available from: https://cds.climate.copernicus.eu/cdsapp#!/home (Accessed 20 June 2020), 2017.

Cunnold, D. M., Zawodny, J. M., Chu, W. P., Pommereau, J. P., Goutail, F., Lenoble, J., McCormick, M. P., Veiga, R. E., Murcray, D., Iwagami, N., Shibasaki, K., Simon, P. C. and Peetermans, W.: Validation of SAGE II NO $_2$ measurements, J. Geophys. Res., 96(D7), 12913, doi:10.1029/91JD01344, 1991.

Dammers, E., McLinden, C. A. C. A., Griffin, D., Shephard, M. W. M. W., Van Der Graaf, S., Lutsch, E., Schaap, M., Gainairu-Matz, Y., Fioletov, V., Van Damme, M., Whitburn, S., Clarisse, L., Cady-Pereira, K., Clerbaux, C., Francois Coheur, P. and Erisman, J.-W. J. W.: NH3 emissions from large point sources derived from CrIS and IASI satellite observations, Atmos. Chem. Phys., 19(19), 12261–12293, doi:10.5194/acp-19-12261-2019, 2019.

https://doi.org/10.5194/acp-2021-536
Preprint. Discussion started: 6 July 2021

Dee, D. P., Uppala, S. M., Simmons, A. J., Berrisford, Poli, P., Kobayashi, S., Andrae, U., Balmaseda, M. A., Balsamo, G., Bauer, P., Bechtold, P., Beljaars, A. C. M., Berg, L. van de, Bidlot, J., Bormann, N., Delsol, C., Dragani, R., Fuentes, M., Geer, A. J., Haimberger, L., Healy, S. B., Hersbach, H., Hólm, E. V., Isaksen, L., Kållberg, P., Köhler, M., Matricardi, M., McNally, A. P., Monge-Sanz, B. M., Morcrette, J.-J., Park, B.-K., Peubey, C., Rosnay, P. de, Tavolato, C., Thépaut, J.-N. and Vitart, F.: The ERA-Interim reanalysis: Configuration and performance of the data assimilation system, Q. J. R. Meteorol. Soc., 137, 553–597, doi:DOI: 10.1002/qj.828, 2011.

Ding, J., van der A, R. J., Eskes, H. J., Mijling, B., Stavrakou, T., van Geffen, J. H. G. M. and Veefkind, J. P.: NOx Emissions Reduction and Rebound in China Due to the COVID-19 Crisis, Geophys. Res. Lett., 47(19), e2020GL089912, doi:10.1029/2020GL089912, 2020.

Duncan, B. N., Lamsal, L. N., Thompson, A. M., Yoshida, Y., Lu, Z., Streets, D. G., Hurwitz, M. M. and Pickering, K. E.: A space-based, high-resolution view of notable changes in urban NOx pollution around the world (2005–2014), J. Geophys. Res. Atmos., 121(X), 976–996, doi:10.1002/2015JD024121.Received, 2015.

EC: European Commission: COVID-19 in European coal regions. [online] Available from: https://ec.europa.eu/energy/sites/ener/files/documents/covid-19_in_european_coal_regions.pdf (Accessed 1 Marchy 2021), 2020.

EPA: U.S. Environmental Protection Agency (EPA) National Emissions Inventory, [online] Available from: https://www.epa.gov/air-emissions-inventories (Accessed 17 July 2020), 2020.

Fioletov, V., McLinden, C. A., Kharol, S. K., Krotkov, N. A., Li, C., Joiner, J., Moran, M. D., Vet, R., Visschedijk, A. J. H. and Denier Van Der Gon, H. A. C.: Multi-source SO2 emission retrievals and consistency of satellite and surface measurements with reported emissions, Atmos. Chem. Phys., 17(20), doi:10.5194/acp-17-12597-2017, 2017.

Fioletov, V. E., McLinden, C. A., Krotkov, N. and Li, C.: Lifetimes and emissions of SO2 from point sources estimated from OMI, Geophys. Res. Lett., 42(6), doi:10.1002/2015GL063148, 2015.

Fioletov, V. E., McLinden, C. A., Krotkov, N. A., Li, C., Joiner, J., Theys, N., Carn, S. and Moran, M. D.: A global catalogue of large SO2 sources and emissions derived from the Ozone Monitoring Instrument, Atmos. Chem. Phys., 16(18), 11497–11519, doi:doi:10.5194/acp-16-11497-2016, 2016.

de Foy, B., Wilkins, J. L., Lu, Z., Streets, D. G. and Duncan, B. N.: Model evaluation of methods for estimating surface emissions and chemical lifetimes from satellite data, Atmos. Environ., 98, 66–77, doi:10.1016/j.atmosenv.2014.08.051, 2014.

de Foy, B., Lu, Z., Streets, D. G., Lamsal, L. N. and Duncan, B. N.: Estimates of power plant NOx emissions and lifetimes from OMI NO2 satellite retrievals, Atmos. Environ., 116, 1–11, doi:10.1016/j.atmosenv.2015.05.056, 2015.

van Geffen, J. H. G. M., Eskes, H. J., Boersma, K. F., Maasakkers, J. D. and Veefkind, J. P.: TROPOMI ATBD of the total and tropospheric NO2 data products., [online] Available from: http://www.tropomi.eu/sites/default/files/files/publicS5P-KNMI-L2-0005-RP-ATBD_NO2_data_products-20190206_v140.pdf (Accessed 17 June 2020), 2019.

https://doi.org/10.5194/acp-2021-536
Preprint. Discussion started: 6 July 2021

Van Geffen, J., Eskes, H., Boersma, K., Maasakkers, J. and Veefkind, J.: TROPOMI ATBD of the total and tropospheric NO2 data products(issue 1.2. 0), De Bilt, the Netherlands, s5P-KNMI-L2-0005-RP., 2018.

Van Geffen, J., Folkert Boersma, K., Eskes, H., Sneep, M., Ter Linden, M., Zara, M. and Pepijn Veefkind, J.: S5P TROPOMI NO2 slant column retrieval: Method, stability, uncertainties and comparisons with OMI, Atmos. Meas. Tech., 13(3), 1315–1335, doi:10.5194/amt-13-1315-2020, 2020.

Georgoulias, A. K., Boersma, K. F., Vliet, J. van, Zhang, X., A1, R. van der, Zanis, P. and Laat, J. de: Detection of NO2 pollution plumes from individual ships with the TROPOMI/S5P satellite sensor, Environ. Res. Lett., 10(2), 0–6, 2020.

Ghahremanloo, M., Lops, Y., Choi, Y. and Mousavinezhad, S.: Impact of the COVID-19 outbreak on air pollution levels in East Asia, Sci. Total Environ., 754, doi:10.1016/j.scitotenv.2020.142226, 2021.

Gkatzelis, G. I., Gilman, J. B., Brown, S. S., Eskes, H., Gomes, A. R., Lange, A. C., McDonald, B. C., Peischl, J., Petzold, A., Thompson, C. R. and Kiendler-Scharr, A.: The global impacts of COVID-19 lockdowns on urban air pollution: A critical review and recommendations, Elementa, 9(1), doi:10.1525/elementa.2021.00176, 2021.

Goldberg, D. L., Anenberg, S. C., Griffin, D., McLinden, C. A., Lu, Z. and Streets, D. G.: Disentangling the impact of the COVID-19 lockdowns on urban NO2 from natural variability, Geophys. Res. Lett., doi:10.1029/2020GL089269, 2020.

Griffin, D., McLinden, C. A., Racine, J., Moran, M. D., Fioletov, V., Pavlovic, R., Mashayekhi, R., Zhao, X. and Eskes, H.: Assessing the impact of corona-virus-19 on nitrogen dioxide levels over southern Ontario, Canada, Remote Sens., 12(24), 1–13, doi:10.3390/rs12244112, 2020.

Guevara, M., Jorba, O., Soret, A., Petetin, H., Bowdalo, D., Serradell, K., Tena, C., Van Der Gon, H. D., Kuenen, J., Peuch, V. H. and Pérez Garciá-Pando, C.: Time-resolved emission reductions for atmospheric chemistry modelling in Europe during the COVID-19 lockdowns, Atmos. Chem. Phys., 21(2), 773–797, doi:10.5194/acp-21-773-2021, 2021.

Hudman, R. C., Moore, N. E., Mebust, A. K., Martin, R. V., Russell, A. R., Valin, L. C. and Cohen, R. C.: Steps towards a mechanistic model of global soil nitric oxide emissions: Implementation and space based-constraints, Atmos. Chem. Phys., 12(16), 7779–7795, doi:10.5194/acp-12-7779-2012, 2012.

Juncosa Calahorrano, J. F., Lindaas, J., O'Dell, K., Palm, B. B., Peng, Q., Flocke, F., Pollack, I. B., Garofalo, L. A., Farmer, D. K., Pierce, J. R., Collett, J. L., Weinheimer, A., Campos, T., Hornbrook, R. S., Hall, S. R., Ullmann, K., Pothier, M. A., Apel, E. C., Permar, W., Hu, L., Hills, A. J., Montzka, D., Tyndall, G., Thornton, J. A. and Fischer, E. V.: Daytime Oxidized Reactive Nitrogen Partitioning in Western U.S. Wildfire Smoke Plumes, J. Geophys. Res. Atmos., 126(4), e2020JD033484, doi:10.1029/2020JD033484, 2021.

Kanniah, K. D., Kamarul Zaman, N. A. F., Kaskaoutis, D. G. and Latif, M. T.: COVID-19's impact on the atmospheric environment in the Southeast Asia region, Sci. Total Environ., 736, 139658, doi:10.1016/j.scitotenv.2020.139658, 2020.

Keller, C. A., Evans, M. J., Emma Knowland, K., Hasenkopf, C. A., Modekurty, S., Lucchesi, R. A., Oda, T., Franca, B. B., Mandarino, F. C., Valeria Díaz Suárez, M., Ryan, R. G., Fakes, L. H. and Pawson, S.: Global impact of COVID-19

https://doi.org/10.5194/acp-2021-536
Preprint. Discussion started: 6 July 2021

restrictions on the surface concentrations of nitrogen dioxide and ozone, Atmos. Chem. Phys., 21(5), 3555–3592, doi:10.5194/acp-21-3555-2021, 2021.

Konovalov, I. B., Beekmann, M., Richter, A. and Burrows, J. P.: Inverse modelling of the spatial distribution of NOX emissions on a continental scale using satellite data, Atmos. Chem. Phys., 6(7), 1747–1770, doi:10.5194/acp-6-1747-2006, 2006.

Koukouli, M. E., Skoulidou, I., Karavias, A., Parcharidis, I., Balis, D., Manders, A., Segers, A., Eskes, H. and Van Geffen, J.: Sudden changes in nitrogen dioxide emissions over Greece due to lockdown after the outbreak of COVID-19, Atmos. Chem. Phys., 21(3), 1759–1774, doi:10.5194/acp-21-1759-2021, 2021.

Krotkov, N. A., McLinden, C. A., Li, C., Lamsal, L. N., Celarier, E. A., Marchenko, S. V., Swartz, W. H., Bucsela, E. J., Joiner, J., Duncan, B. N., Boersma, K. F., Veefkind, J. P., Levelt, P. F., Fioletov, V. E., Dickerson, R. R., He, H., Lu, Z. and Streets, D. G.: Aura OMI observations of regional SO_2 and NO_2 pollution changes from 2005 to 2015, Atmos. Chem. Phys., 16(7), 4605–4629, doi:10.5194/acp-16-4605-2016, 2016.

Lamsal, L. N., Martin, R. V., Parrish, D. D. and Krotkov, N. A.: Scaling relationship for NO2 pollution and urban population size: A satellite perspective, Environ. Sci. Technol., 47(14), 7855–7861, doi:10.1021/es400744g, 2013.

Lamsal, L. N., Duncan, B. N., Yoshida, Y., Krotkov, N. a., Pickering, K. E., Streets, D. G. and Lu, Z.: U.S. NO2 trends (2005–2013): EPA Air Quality System (AQS) data versus improved observations from the Ozone Monitoring Instrument (OMI), Atmos. Environ., 110(2), 130–143, doi:10.1016/j.atmosenv.2015.03.055, 2015.

Lange, K., Richter, A. and Burrows, J. P.: Variability of nitrogen oxide lifetimes and emission fluxes estimated by Sentinel-5P observations, Atmos. Chem. Phys. Discuss., doi:https://doi.org/10.5194/acp-2021-273, 2021.

Laughner, J. and Cohen, R. C.: Direct observation of changing NOx lifetime in North American cities, Science (80-.)., 366(6466), 723–727 [online] Available from: https://science.sciencemag.org/content/366/6466/723.full, 2019.

Levelt, P. F., Joiner, J., Tamminen, J., Veefkind, J. P., Bhartia, P. K., Fioletov, V., Carn, S., Laat, J. De, Deland, M., Marchenko, S. and Mcpeters, R.: The Ozone Monitoring Instrument : overview of 14 years in space, Atmos. Chem. Phys, 18, 5699–5745, doi:https://doi.org/10.5194/acp-18-5699-2018, 2018.

Liu, F., Beirle, S., Zhang, Q., Dörner, S., He, K. and Wagner, T.: NO_x lifetimes and emissions of cities and power plants in polluted background estimated by satellite observations, Atmos. Chem. Phys., 16(8), 5283–5298, doi:10.5194/acp-16-5283-2016, 2016.

Liu, F., Choi, S., Li, C., Fioletov, V. E., Mclinden, C. A. and Joiner, J.: A new global anthropogenic SO 2 emission inventory for the last decade : a mosaic of satellite-derived and bottom-up emissions, Atmos. Chem. Phys., 18, 16571–16586, 2018.

Liu, F., Page, A., Strode, S. A., Yoshida, Y., Choi, S., Zheng, B., Lamsal, L. N., Li, C., Krotkov, N. A., Eskes, H., Ronald Vander, A., Veefkind, P., Levelt, P., Joiner, J. and Hauser, O. P.: Abrupt declines in tropospheric nitrogen dioxide over China after the outbreak of COVID-19, arXiv, (2), 2–7, 2020.

Lorente, A., Boersma, K. F., Eskes, H. J., Veefkind, J. P., van Geffen, J. H. G. M., de Zeeuw, M. B., Denier van der Gon, H.

https://doi.org/10.5194/acp-2021-536
Preprint. Discussion started: 6 July 2021

A. C., Beirle, S. and Krol, M. C.: Quantification of nitrogen oxides emissions from build-up of pollution over Paris with TROPOMI, Sci. Rep., 9(1), 1–10, doi:10.1038/s41598-019-56428-5, 2019.

Lu, Z., Streets, D. G., De Foy, B., Lamsal, L. N., Duncan, B. N. and Xing, J.: Emissions of nitrogen oxides from US urban areas: Estimation from Ozone Monitoring Instrument retrievals for 2005-2014, Atmos. Chem. Phys., 15(18), 10367–10383, doi:10.5194/acp-15-10367-2015, 2015.

Martin, R. V., Chance, K., Jacob, D. J., Kurosu, T. P., Spurr, R. J. D., Bucsela, E., Gleason, J. F., Palmer, P. I., Bey, I., Fiore, A. M., Li, Q., Yantosca, R. M. and Koelemeijer, R. B. A.: An improved retrieval of tropospheric nitrogen dioxide from GOME, J. Geophys. Res. D Atmos., 107(20), doi:10.1029/2001JD001027, 2002.

McLinden, C. A., Fioletov, V., Boersma, K. F., Krotkov, N., Sioris, C. E., Veefkind, J. P. and Yang, K.: Air quality over the Canadian oil sands: A first assessment using satellite observations, Geophys. Res. Lett., 39(4), 1–8, doi:10.1029/2011GL050273, 2012.

McLinden, C. A., Fioletov, V., Shephard, M. W., Krotkov, N., Li, C., Martin, R. V., Moran, M. D. and Joiner, J.: Space-based detection of missing sulfur dioxide sources of global air pollution, Nat. Geosci., 9(7), 496–500, doi:10.1038/ngeo2724, 2016.

McLinden, C. A., Adams, C. L. F., Fioletov, V., Griffin, D., Makar, P. A., Zhao, X., Kovachik, A., Dickson, N. M., Brown, C., Krotkov, N., Li, C., Theys, N., Hedelt, P. and Loyola, D. G.: Inconsistencies in sulphur dioxide emissions from the Canadian oil sands and potential implications, Environ. Res. Lett., 16, doi:10.1088/1748-9326/abcbbb, 2020.

Mijling, B. and Van Der A, R. J.: Using daily satellite observations to estimate emissions of short-lived air pollutants on a mesoscopic scale, J. Geophys. Res. Atmos., 117(17), 17302, doi:10.1029/2012JD017817, 2012.

Miller, S. D., Mills, S. P., Elvidge, C. D., Lindsey, D. T., Lee, T. F. and Hawkins, J. D.: Suomi satellite brings to light a unique frontier of nighttime environmental sensing capabilities, Proc. Natl. Acad. Sci. U. S. A., 109(39), 15706–15711, doi:10.1073/pnas.1207034109, 2012.

NOAA: 2-Minute Gridded Global Relief Data (ETOPO2v2), [online] Available from: https://www.ngdc.noaa.gov/mgg/global/etopo2.html (Accessed 17 June 2020), 2006.

NPRI: National Pollutant Release Inventory (NPRI). Sulfur oxide emissions for Canada, [online] Available from: www.canada.ca/en/services/environment/pollution-waste-management/national-pollutant-release-inventory.html (Accessed 17 July 2020), 2020.

Pommier, M., McLinden, C. A. and Deeter, M.: Relative changes in CO emissions over megacities based on observations from space, Geophys. Res. Lett., 40(14), 3766–3771, doi:10.1002/grl.50704, 2013.

Qu, Z., Jacob, D. J., Silvern, R. F., Shah, V., Campbell, P. C., Valin, L. C. and Murray, L. T.: US COVID-19 shutdown demonstrates importance of background NO2 in inferring NOx emissions from satellite NO2 observations, Geophys. Res. Lett., 48(10), doi:10.1029/2021GL092783, 2021.

Richter, A., Eyring, V., Burrows, J. P., Bovensmann, H., Lauer, A., Sierk, B. and Crutzen, P. J.: Satellite measurements of NO2 from international shipping emissions, Geophys. Res. Lett., 31(23), 1–4, doi:10.1029/2004GL020822, 2004.

https://doi.org/10.5194/acp-2021-536
Preprint. Discussion started: 6 July 2021

SEDAC: The Gridded Population of the World (GPW), [online] Available from: https://sedac.ciesin.columbia.edu/data/collection/gpw-v4, 2017.

Sha, T., Ma, X., Zhang, H., Janechek, N., Wang, Y., Wang, Y., Castro Garciá, L., Jenerette, G. D. and Wang, J.: Impacts of Soil NOxEmission on O3Air Quality in Rural California, Environ. Sci. Technol., doi:10.1021/acs.est.0c06834, 2021.

Silvern, R. F., Jacob, D. J., Mickley, L. J., Sulprizio, M. P., Travis, K. R., Marais, E. A., Cohen, R. C., Laughner, J. L., Choi, S., Joiner, J. and Lamsal, L. N.: Using satellite observations of tropospheric NO2 columns to infer long-term trends in US NOx emissions: The importance of accounting for the free tropospheric NO2 background, Atmos. Chem. Phys., 19(13), 8863–8878, doi:10.5194/acp-19-8863-2019, 2019.

Stavrakou, T., Müller, J. F., Bauwens, M., Boersma, K. F. and van Geffen, J.: Satellite evidence for changes in the NO2 weekly cycle over large cities, Sci. Rep., 10(1), 1–9, doi:10.1038/s41598-020-66891-0, 2020.

Streets, D. G., Canty, T., Carmichael, G. R., De Foy, B., Dickerson, R. R., Duncan, B. N., Edwards, D. P., Haynes, J. A., Henze, D. K., Houyoux, M. R., Jacob, D. J., Krotkov, N. A., Lamsal, L. N., Liu, Y., Lu, Z., Martin, R. V., Pfister, G. G., Pinder, R. W., Salawitch, R. J. and Wecht, K. J.: Emissions estimation from satellite retrievals: A review of current capability, Atmos. Environ., 77, 1011–1042, doi:10.1016/j.atmosenv.2013.05.051, 2013.

Vadrevu, K. P., Eaturu, A., Biswas, S., Lasko, K., Sahu, S., Garg, J. K. and Justice, C.: Spatial and temporal variations of air pollution over 41 cities of India during the COVID-19 lockdown period, Sci. Rep., 10(1), 1–15, doi:10.1038/s41598-020-72271-5, 2020.

Veefkind, J. P. P., Aben, I., McMullan, K., Förster, H., de Vries, J., Otter, G., Claas, J., Eskes, H. J. J., de Haan, J. F. F., Kleipool, Q., van Weele, M., Hasekamp, O., Hoogeveen, R., Landgraf, J., Snel, R., Tol, P., Ingmann, P., Voors, R., Kruizinga, B., Vink, R., Visser, H. and Levelt, P. F. F.: TROPOMI on the ESA Sentinel-5 Precursor: A GMES mission for global observations of the atmospheric composition for climate, air quality and ozone layer applications, Remote Sens. Environ., 120(2012), 70–83, doi:10.1016/j.rse.2011.09.027, 2012.

Verhoelst, T., Compernolle, S., Pinardi, G., Lambert, J. C., Eskes, H. J., Eichmann, K. U., Fjæraa, A. M., Granville, J., Niemeijer, S., Cede, A., Tiefengraber, M., Hendrick, F., Pazmiño, A., Bais, A., Bazureau, A., Folkert Boersma, K., Bognar, K., Dehn, A., Donner, S., Elokhov, A., Gebetsberger, M., Goutail, F., Grutter De La Mora, M., Gruzdev, A., Gratsea, M., Hansen, G. H., Irie, H., Jepsen, N., Kanaya, Y., Karagkiozidis, D., Kivi, R., Kreher, K., Levelt, P. F., Liu, C., Müller, M., Navarro Comas, M., Piters, A. J. M., Pommereau, J. P., Portafaix, T., Prados-Roman, C., Puentedura, O., Querel, R., Remmers, J., Richter, A., Rimmer, J., Cárdenas, C. R., De Miguel, L. S., Sinyakov, V. P., Stremme, W., Strong, K., Van Roozendael, M., Pepijn Veefkind, J., Wagner, T., Wittrock, F., Yela González, M. and Zehner, C.: Ground-based validation of the Copernicus Sentinel-5P TROPOMI NO2 measurements with the NDACC ZSL-DOAS, MAX-DOAS and Pandonia global networks, Atmos. Meas. Tech., 14(1), 481–510, doi:10.5194/amt-14-481-2021, 2021.

Vinnikov, K. Y., Dickerson, R. R., Krotkov, N. A., Edgerton, E. S. and Schwab, J. J.: The net decay time of anomalies in concentrations of atmospheric pollutants, Atmos. Environ., 160, 19–26, doi:10.1016/j.atmosenv.2017.04.006, 2017.

https://doi.org/10.5194/acp-2021-536
Preprint. Discussion started: 6 July 2021

Vîrghileanu, M., Săvulescu, I., Mihai, B. A., Nistor, C. and Dobre, R.: Nitrogen dioxide (No2) pollution monitoring with sentinel-5p satellite imagery over europe during the coronavirus pandemic outbreak, Remote Sens., 12(21), 1–29, doi:10.3390/rs12213575, 2020.

Williams, J. E., Folkert Boersma, K., Le Sager, P. and Verstraeten, W. W.: The high-resolution version of TM5-MP for optimized satellite retrievals: Description and validation, Geosci. Model Dev., 10(2), 721–750, doi:10.5194/gmd-10-721-2017, 2017.

Zhang, H., Lin, Y., Wei, S., Loo, B. P. Y., Lai, P. C., Lam, Y. F., Wan, L. and Li, Y.: Global association between satellite-derived nitrogen dioxide (NO2) and lockdown policies under the COVID-19 pandemic, Sci. Total Environ., 761, 144148, doi:10.1016/j.scitotenv.2020.144148, 2021.

Zoogman, P., Liu, X., Suleiman, R. M., Pennington, W. F., Flittner, D. E., Al-Saadi, J. A., Hilton, B. B., Nicks, D. K., Newchurch, M. J., Carr, J. L., Janz, S. J., Andraschko, M. R., Arola, A., Baker, B. D., Canova, B. P., Chan Miller, C., Cohen, R. C., Davis, J. E., Dussault, M. E., Edwards, D. P., Fishman, J., Ghulam, A., González Abad, G., Grutter, M., Herman, J. R., Houck, J., Jacob, D. J., Joiner, J., Kerridge, B. J., Kim, J., Krotkov, N. A., Lamsal, L., Li, C., Lindfors, A., Martin, R. V., McElroy, C. T., McLinden, C., Natraj, V., Neil, D. O., Nowlan, C. R., O'Sullivan, E. J., Palmer, P. I., Pierce, R. B., Pippin, M. R., Saiz-Lopez, A., Spurr, R. J. D., Szykman, J. J., Torres, O., Veefkind, J. P., Veihelmann, B., Wang, H., Wang, J. and Chance, K.: Tropospheric emissions: Monitoring of pollution (TEMPO), J. Quant. Spectrosc. Radiat. Transf., doi:10.1016/j.jqsrt.2016.05.008, 2016.

https://doi.org/10.5194/acp-2021-536
Preprint. Discussion started: 6 July 2021

Atmospheric Chemistry and Physics Discussions

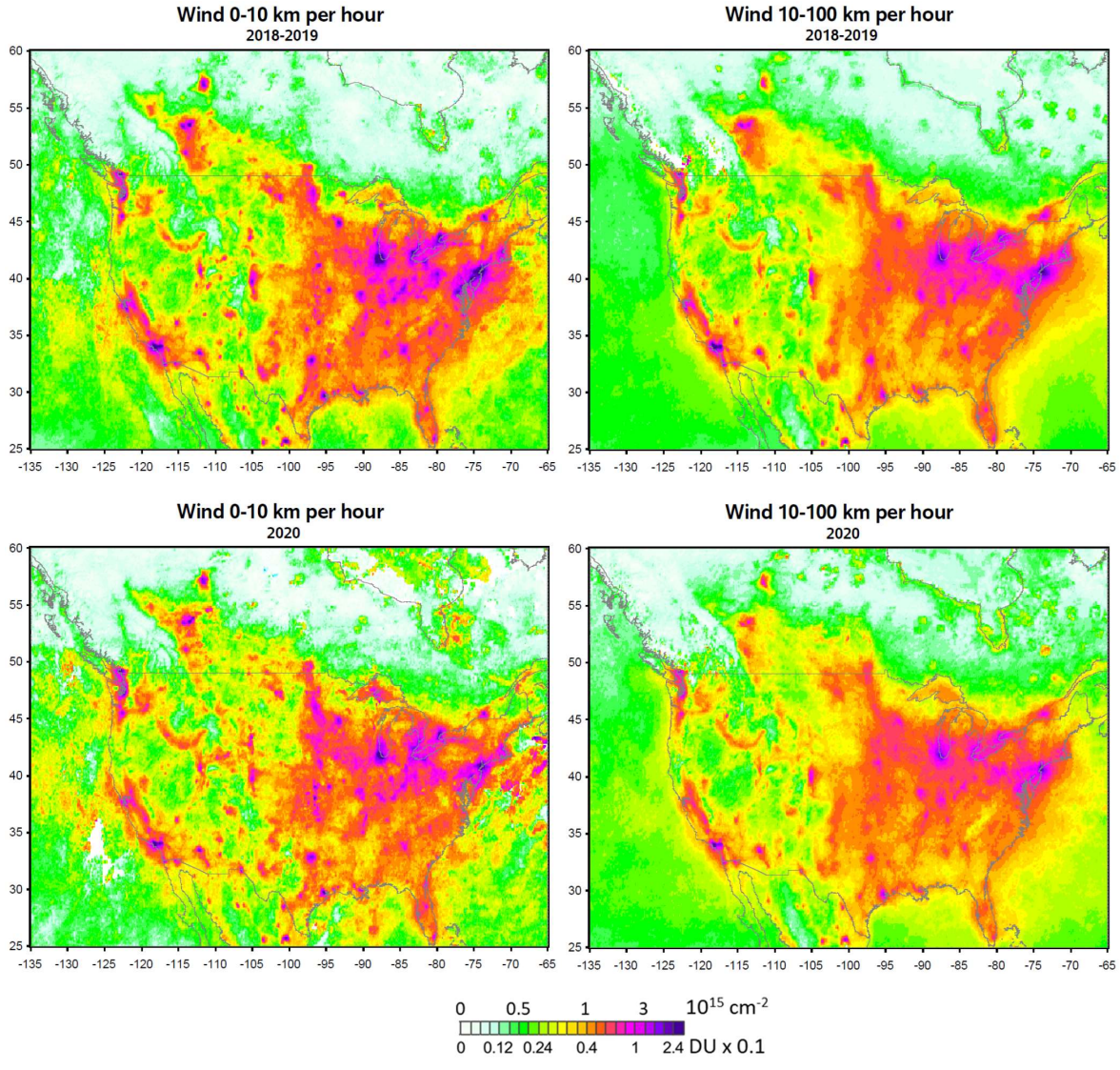

Figure 1. Mean TROPOMI NO_2 VCDs over the US and southern Canada for March 16–June 15, in 2018-2019 and 2020. The main features of the NO_2 distribution such as elevated NO_2 values over large cities, industrial sources and lower values over the mountains are evident from the plot. Also, NO_2 VCDs are not negligible over remote areas suggesting some background levels.

https://doi.org/10.5194/acp-2021-536
Preprint. Discussion started: 6 July 2021

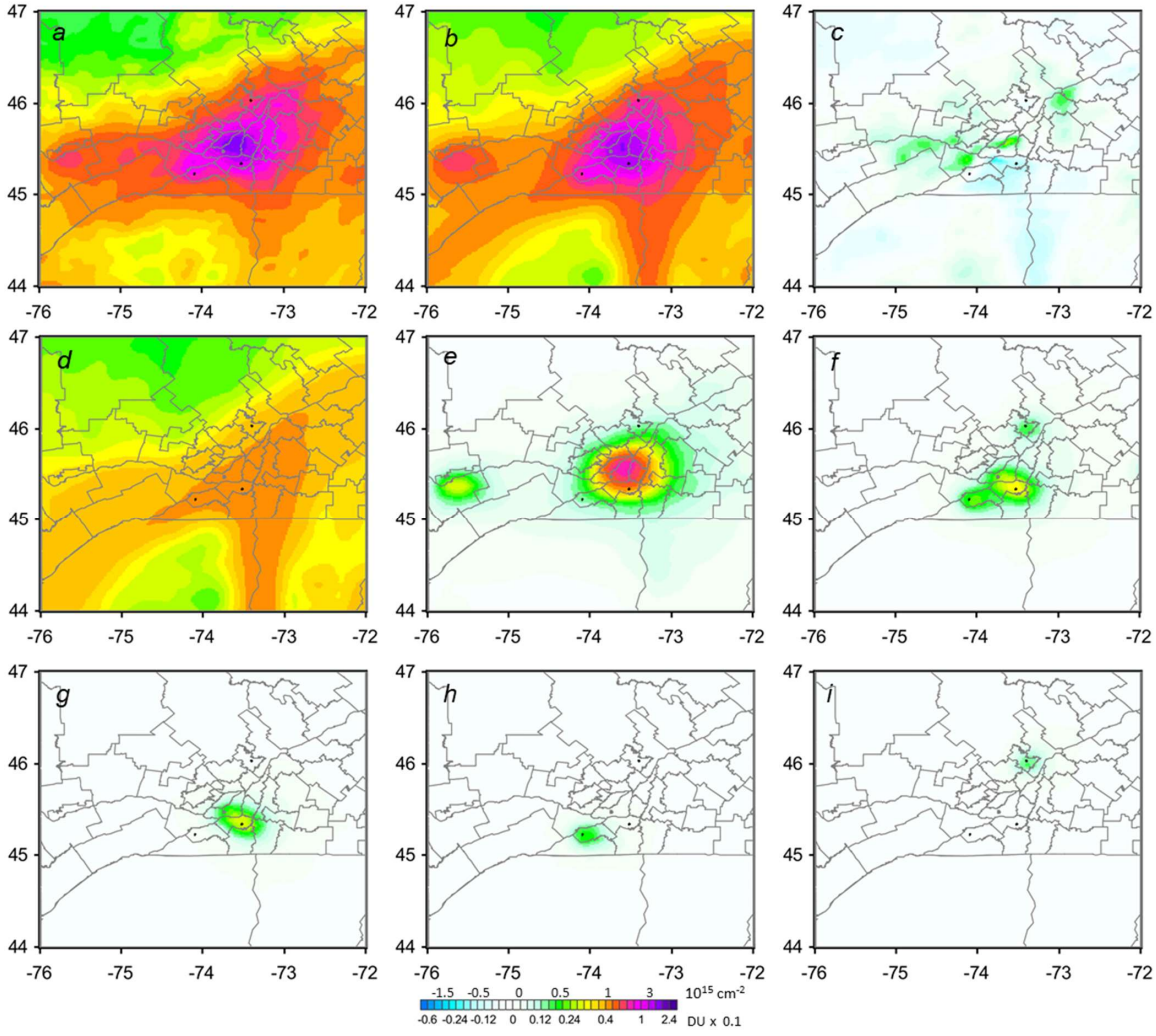

Figure 2. (*a*) Mean TROPOMI NO_2 for March 16– June 15, 2018-2019, over the Montreal area, (*b*) the fitting results and (*c*) the residuals (i.e., the difference between (*a*) and (*b*)). Tropospheric NO_2 VCDs have a large "background" level that is reflected by (*d*) the elevation-related component. (*e*) The population density-related and (*f*) industrial sources-related components. Emission point sources are shown by the black dots. The industrial sources-related component is comprised of three clusters: one (*g*) with two sources and two (*h, i*) with one source each. The data are smoothed by the oversampling technique with the averaging radius R=10 km. Panel (*b*) is the sum of panels (*d*), (*e*) and (*f*).

https://doi.org/10.5194/acp-2021-536
Preprint. Discussion started: 6 July 2021

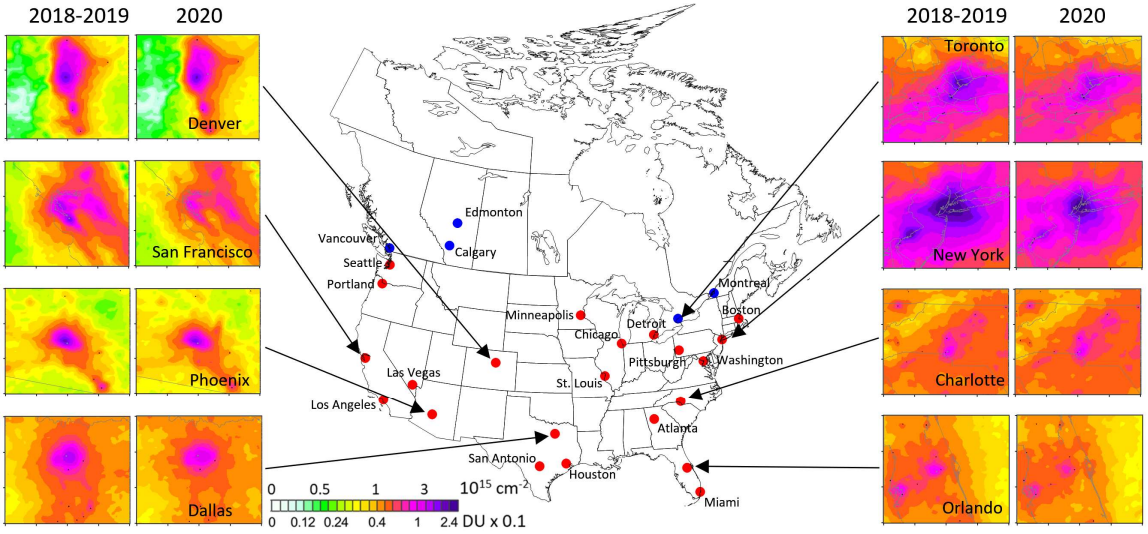

Figure 3. The map of locations of the analysed 27 most populated urban cites in (red) the US and (blue) Canada (22 and 5 areas respectively). The analysis was done for 3° (latitude) by 4°(longitude) areas around the sites. The mean NO_2 values for the period from March 16 to June 15 in 2018-2019 and 2020 are shown.

https://doi.org/10.5194/acp-2021-536
Preprint. Discussion started: 6 July 2021

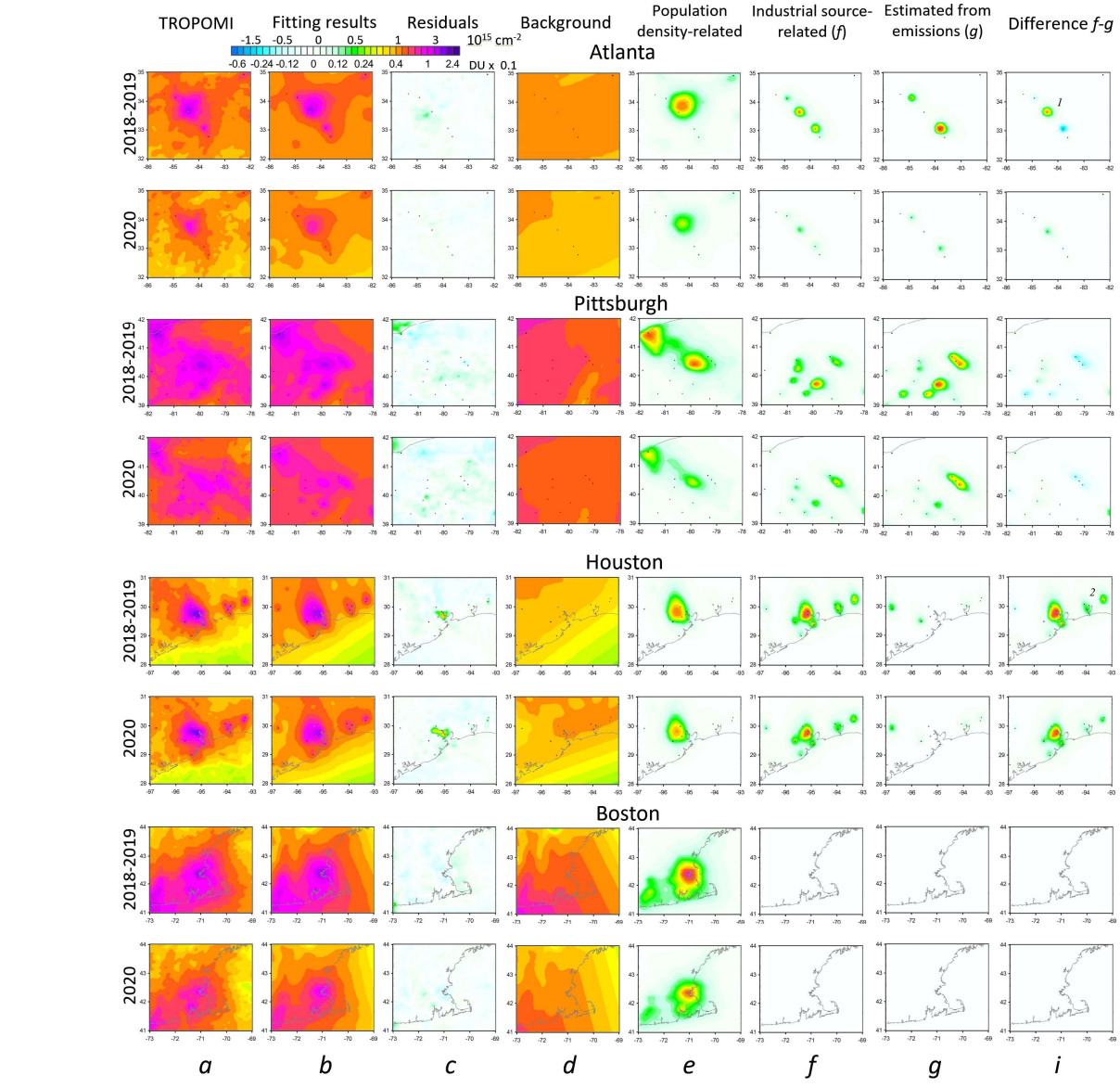

Figure 4. Mean TROPOMI NO_2 for March 16–June 15 over the four areas as indicated. The columns represent: mean TROPOMI NO_2 values, (column *a*), the fitting results (*b*), the residuals (*c*) and well as individual components of the fitting: the elevation-related (*d*), the population density-related (*e*), and the industrial sources-related (*f*). VCDs estimated from

https://doi.org/10.5194/acp-2021-536
Preprint. Discussion started: 6 July 2021


Atmospheric Chemistry and Physics Discussions

reported emissions are in column (*g*) and the difference between columns *f* and *g* is in column *i*. *1*- Hartsfield–Jackson Atlanta International Airport, *2*- oil refineries near Houston.

https://doi.org/10.5194/acp-2021-536
Preprint. Discussion started: 6 July 2021

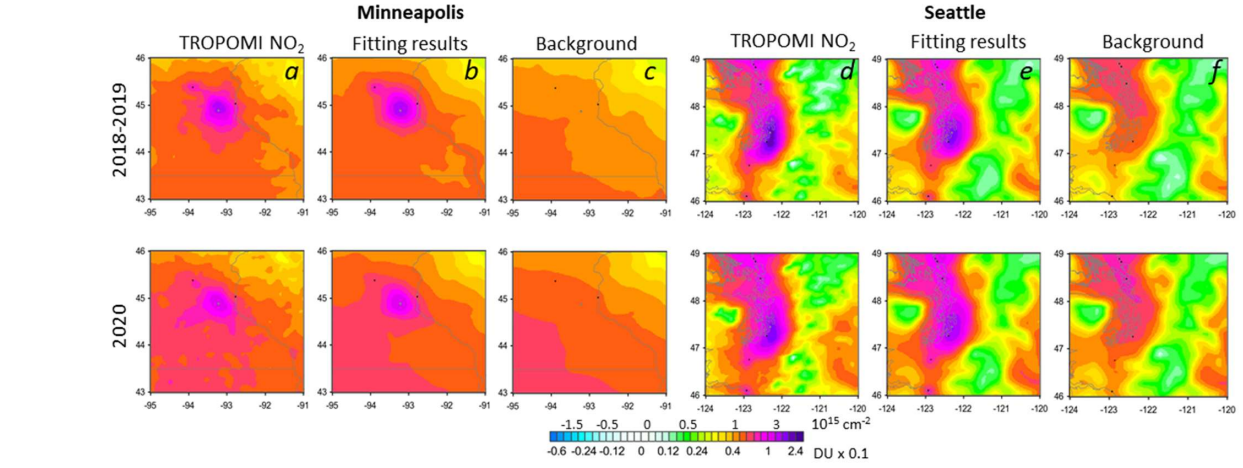

Figure 5. Mean TROPOMI NO_2 for March 16 – June 15 over a flat area around Minneapolis and mountain area around Seattle as indicated. The columns represent: mean TROPOMI NO_2 values, (column *a, d*), the fitting results (*b, e*), and the elevation-related background component (*c, f*).

https://doi.org/10.5194/acp-2021-536
Preprint. Discussion started: 6 July 2021

Atmospheric Chemistry and Physics Discussions

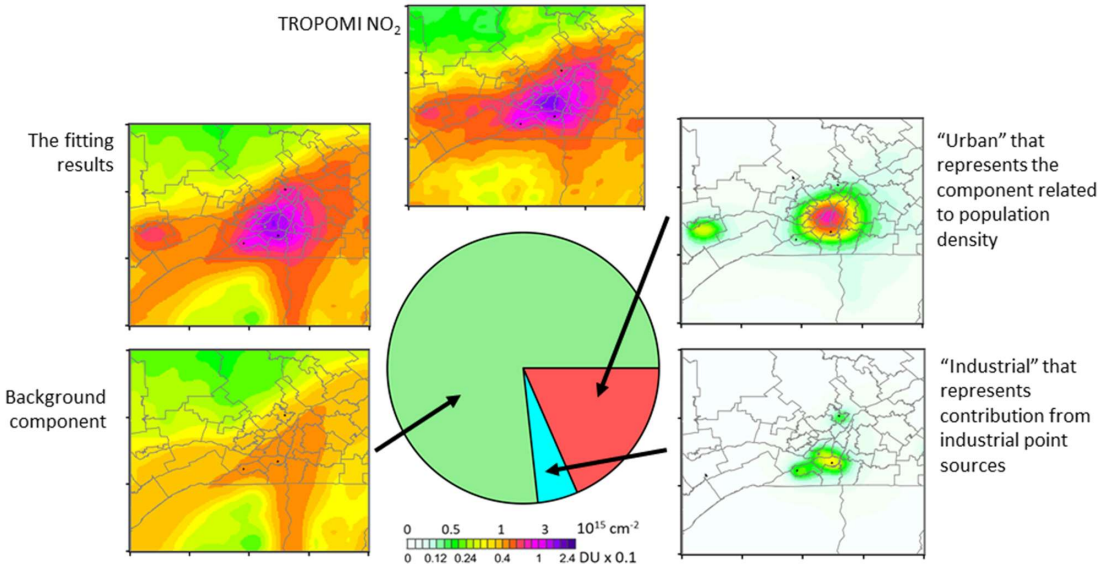

Figure 6. The contribution of the three components to the total NO_2 mass in the Montreal area for March 16 – June 15 (average for 2018-2019). The total mass can be represented as a sum of three components shown in Figure 2.

5

https://doi.org/10.5194/acp-2021-536
Preprint. Discussion started: 6 July 2021

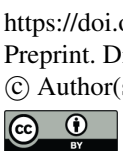

Atmospheric Chemistry and Physics Discussions

Figure 7. Relative contribution of the three components (background, urban, and industrial) components for all 27 Canadian and U.S. areas for March 16 – June 15 (average for 2018-2019). The contribution from industrial sources and cities are responsible for less than a third of total NO_2 mass of the analysed 3° by 4° urban areas.

5

https://doi.org/10.5194/acp-2021-536
Preprint. Discussion started: 6 July 2021

Atmospheric Chemistry and Physics Discussions

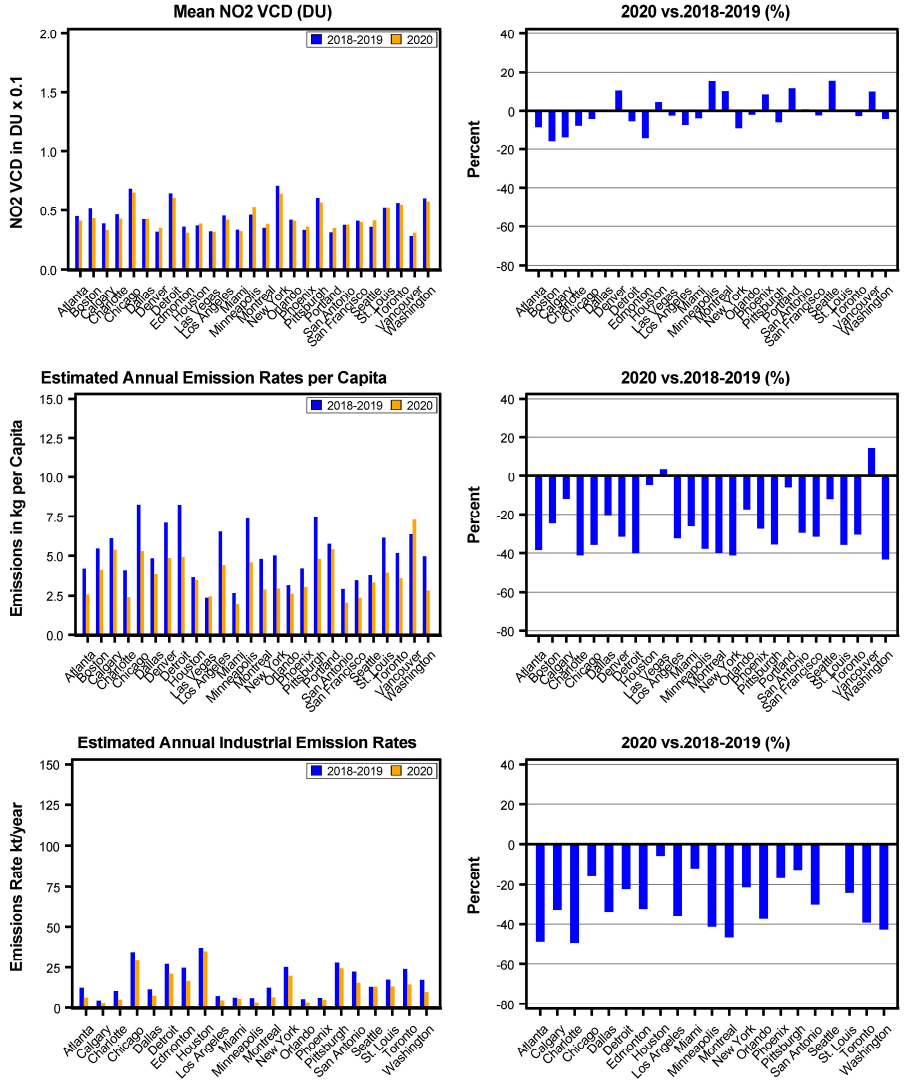

Figure 8. (left) The mean values for March 16– June 15 in 2018-2019 (blue) and 2020 (orange) values for the three components for the (top) background, (middle) urban, and (bottom) industrial components for all 27 analysed areas. (right) The decline 2020 mean values in percent from the mean 2018-2019 values.

5

https://doi.org/10.5194/acp-2021-536
Preprint. Discussion started: 6 July 2021

Atmospheric Chemistry and Physics Discussions

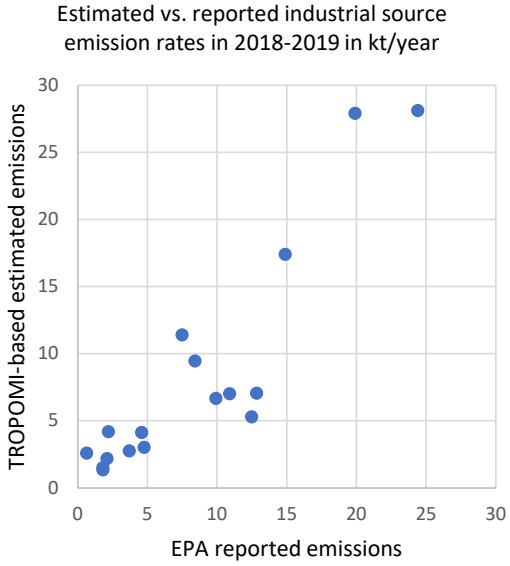

Figure 9. Estimated and reported annual NO_2 emissions rates for 2018-2019. Each dot represents the sum of all emissions in one urban area. The emissions are expressed as annual rates. TROPOMI emissions were calculated only for the sites that reported their emissions. The correlation coefficient between the two data sets is 0.9. Areas that have no reported emissions data for 2019 are not included in the plot.

https://doi.org/10.5194/acp-2021-536
Preprint. Discussion started: 6 July 2021

Atmospheric Chemistry and Physics Discussions

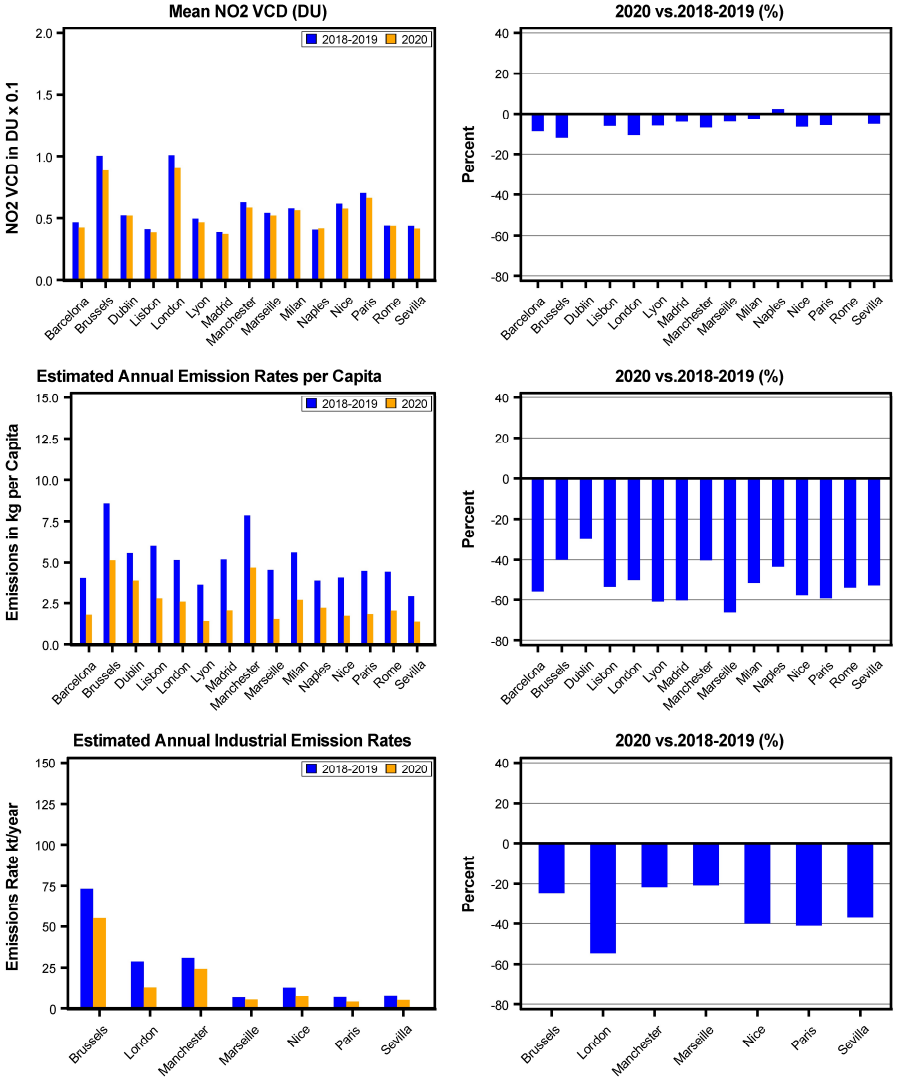

5 **Figure 10a.** The same as Fig. 8, but for Europe-1 sub-region (Italy, France, Spain, Portugal, Belgium, Ireland, and UK).

https://doi.org/10.5194/acp-2021-536
Preprint. Discussion started: 6 July 2021

Atmospheric Chemistry and Physics Discussions

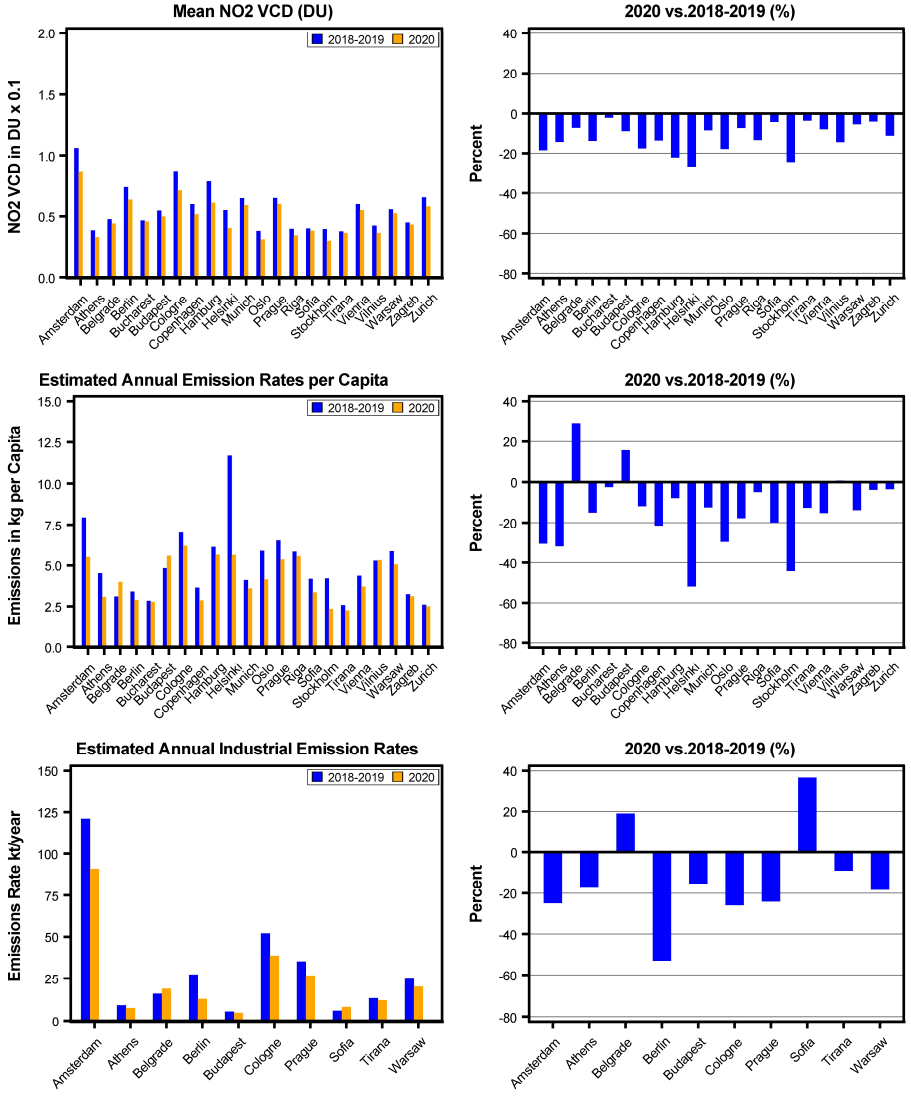

Figure 10b. The same as Fig. 8, but for Europe-2 sub-region (other EU countries and non-members from former Yugoslavia).

5

https://doi.org/10.5194/acp-2021-536
Preprint. Discussion started: 6 July 2021

Atmospheric Chemistry and Physics Discussions

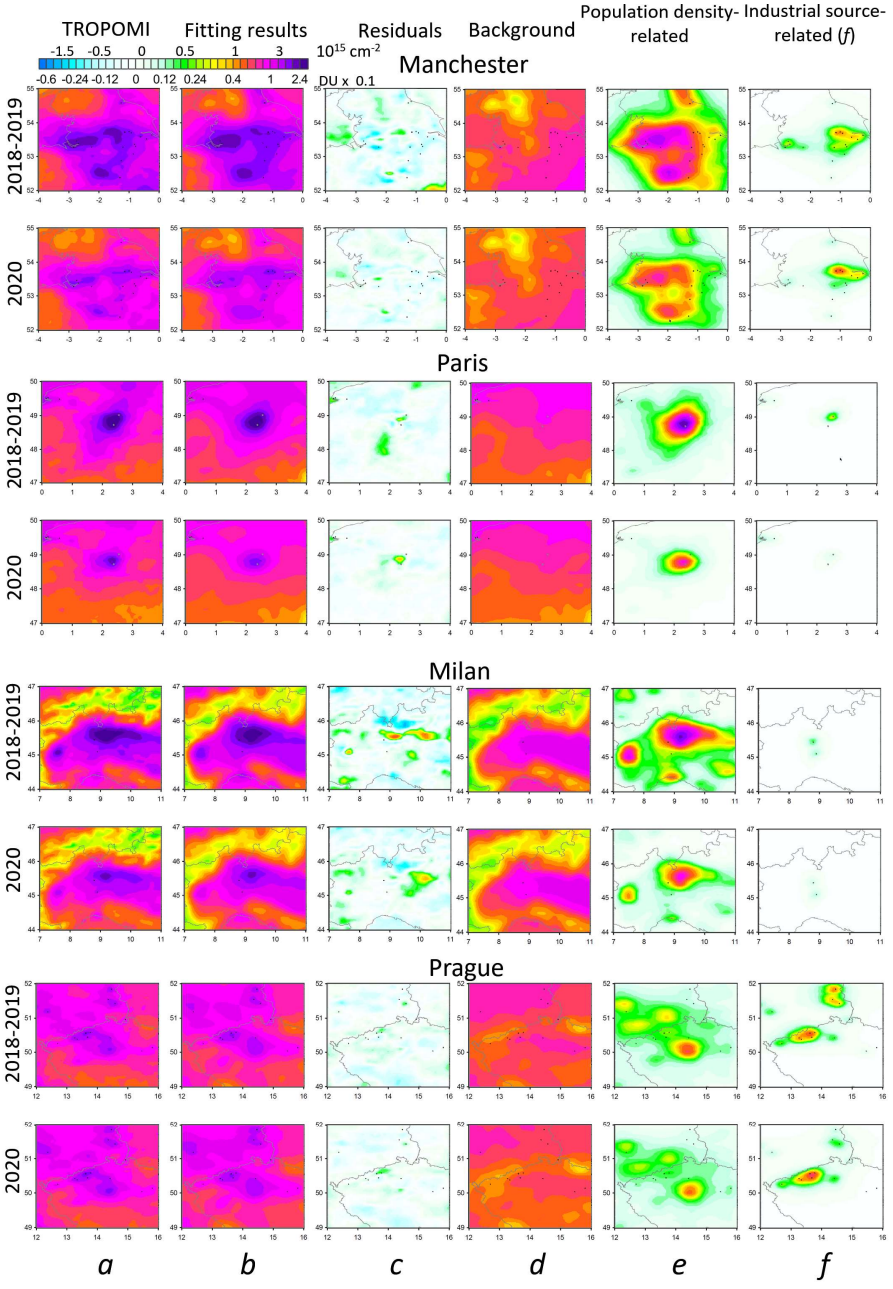

Figure 11. Similar to Figure 4 columns a-f, for areas around four European cities: Manchester, Paris, Milan, and Prague.

https://doi.org/10.5194/acp-2021-536
Preprint. Discussion started: 6 July 2021

Atmospheric Chemistry and Physics Discussions

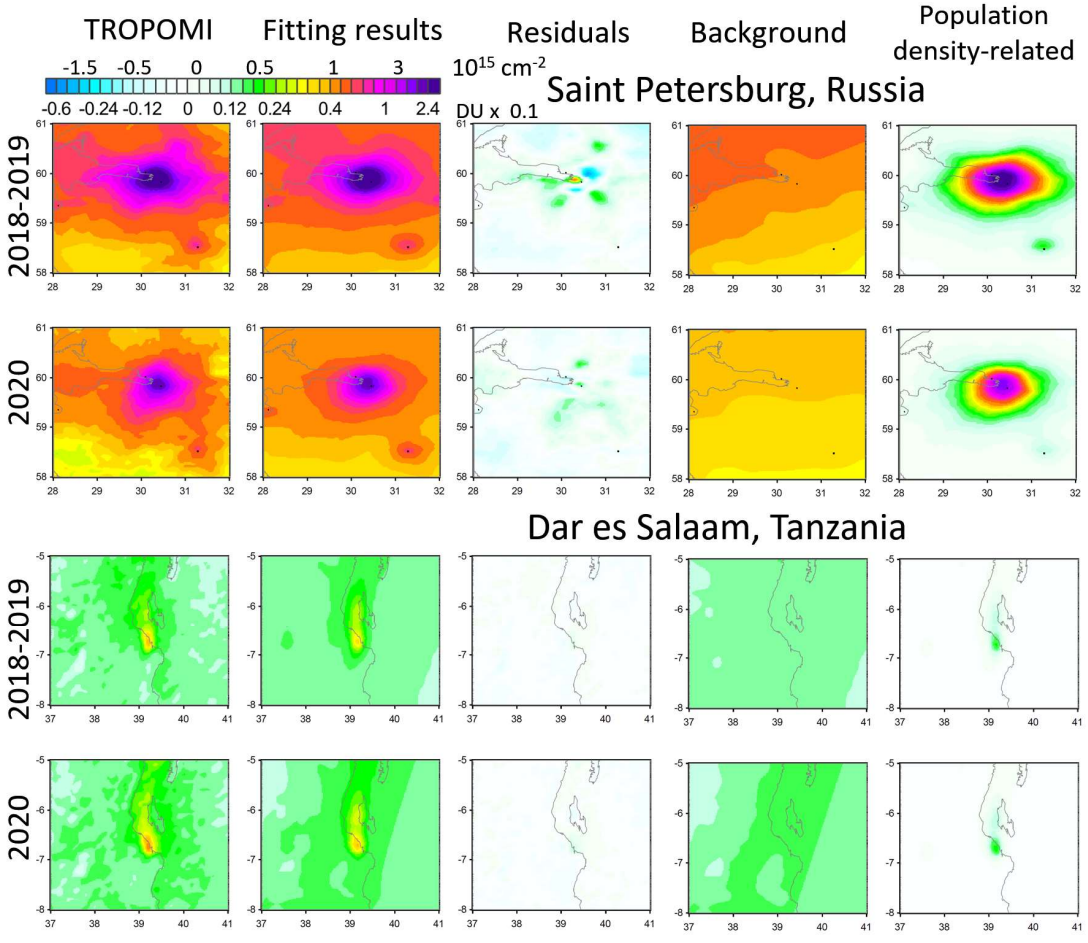

Figure 12. Similar to Figure 4 columns a-e, for Saint Petersburg, and Dar es Salaam, cities with similar population of about 6 million people, but very different NO_2 "footprint". There are no large industrial sources in these two areas.

https://doi.org/10.5194/acp-2021-536
Preprint. Discussion started: 6 July 2021

Atmospheric Chemistry and Physics Discussions

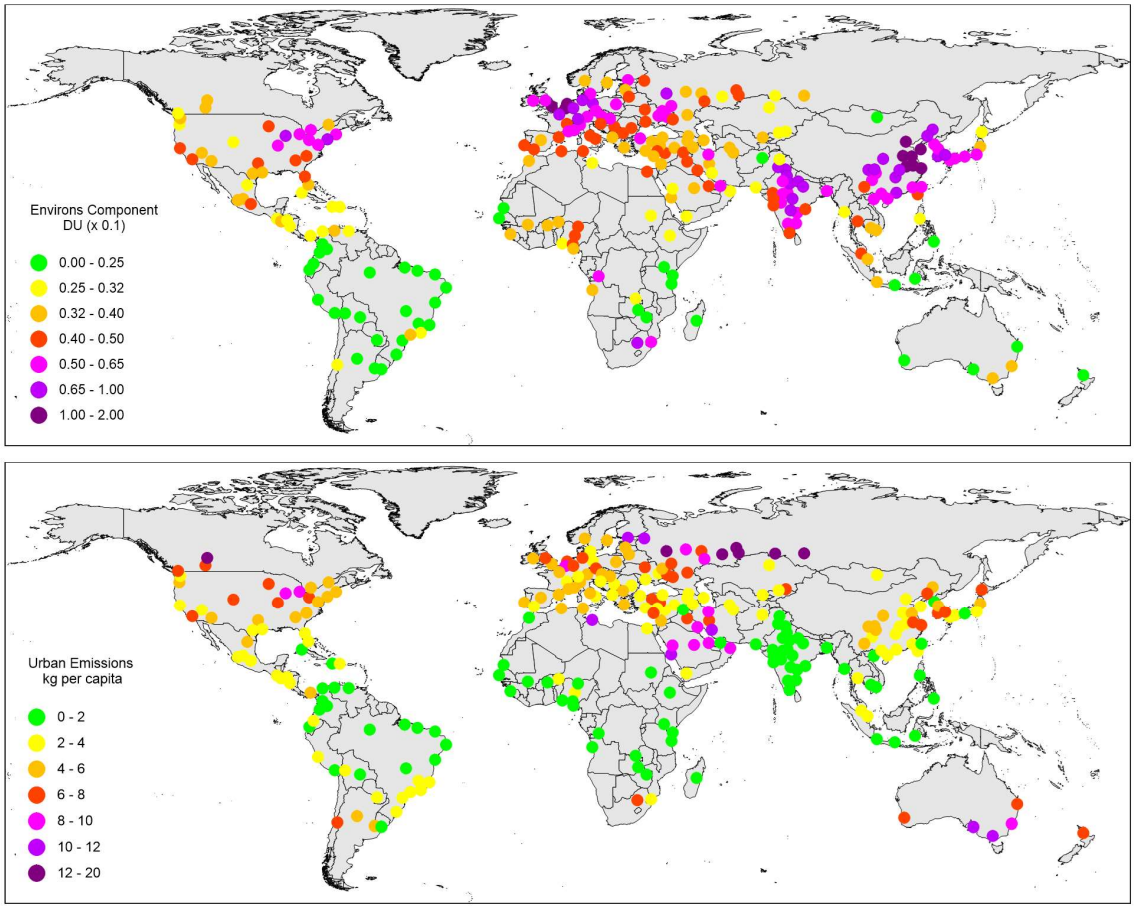

Figure 13. (top) The map of the background component NO_2 in 2018-2019 for the period March 16 – June 15 estimated from TROPOMI. (bottom) The map of emissions per capita for the same period. The analysis was done using estimates for large cities (> 1 million).

https://doi.org/10.5194/acp-2021-536
Preprint. Discussion started: 6 July 2021

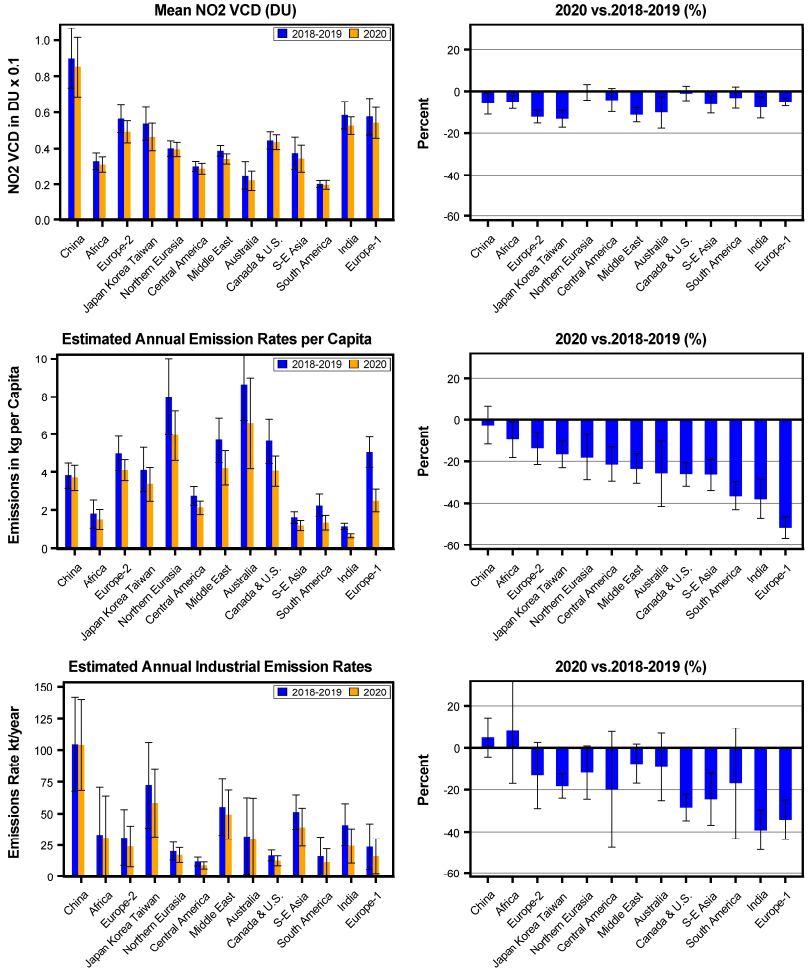

Figure 14. (left) The mean values for March 16–June 15 in 2018-2019 (blue) and 2020 (orange) values for the three components for the (top) background-, (middle) urban-, and (bottom) industrial components for the 13 regions. (right) The decline 2020 mean values in percent from the mean 2018-2019 values. The data are sorted according to the changes between 2020 and 2018-2019 in the urban component (middle right panel). The error bars represent 2σ intervals. Mean values for each region were calculated as a mean of all areas for that region. The uncertainty was calculated as a standard error of the mean.

https://doi.org/10.5194/acp-2021-536
Preprint. Discussion started: 6 July 2021

Atmospheric Chemistry and Physics Discussions

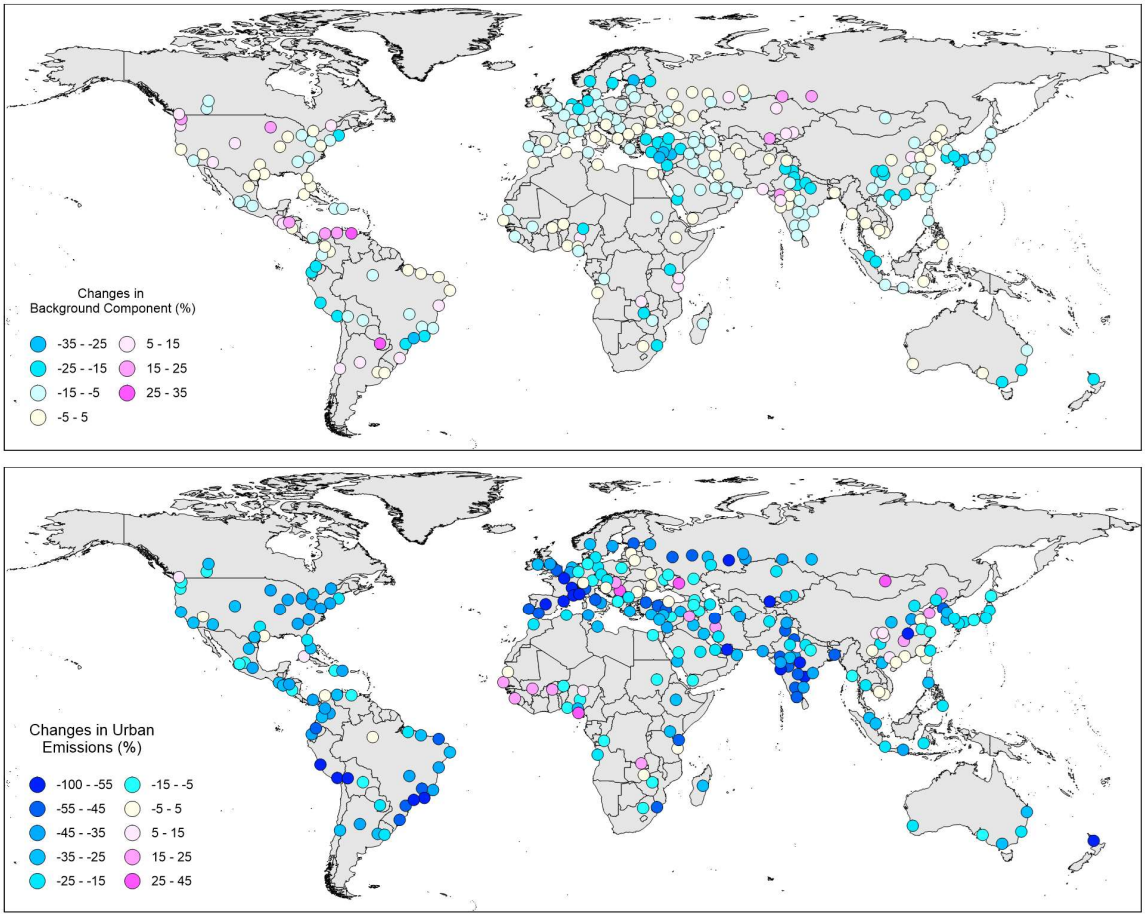

Figure 15. The map of NO_2 percent changes between 2018-2019 and 2020 for the period March 16 – June 15 estimated from TROPOMI data for (top) background component and (bottom) urban emissions per capita. The analysis was done using estimates for large cities (> 1 million).

https://doi.org/10.5194/acp-2021-536
Preprint. Discussion started: 6 July 2021

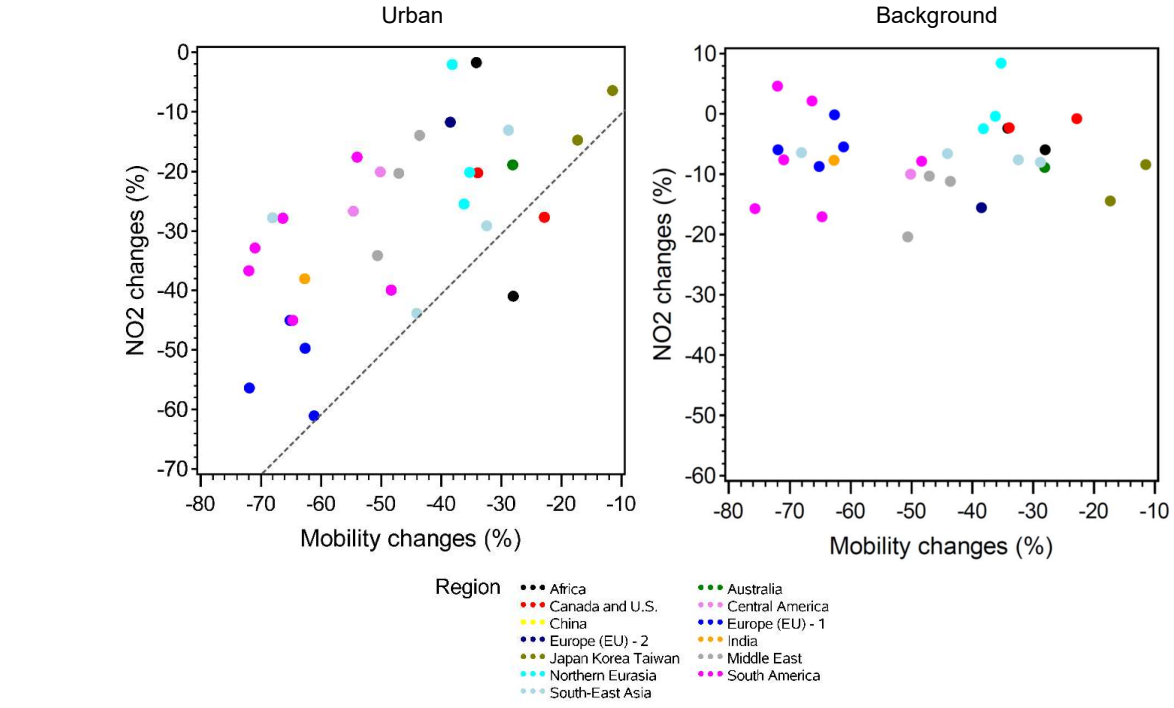

Figure 16. (left) A scatter plot of Google mobility statistic (for "retail and recreation" sites) changes vs. TROPOMI NO_2 VCD changes for the urban (population density-related) component during the period from March 16 to June 15. The Google mobility statistic changes show the difference with the pre-lockdown period in percent. For TROPOMI, the difference is between the 2020 values and the average for the 2018-2019 average. Each dot represents one country, the dot colour demonstrates the region as shown in the legend. Only countries with at least two cities used in this study are included in this plot. The correlation coefficient between the two data sets is 0.66. The dashed Y=X line is shown for reference. (right) The same plot, but for the background component.